Journal of Structural Geology 205 (2026) 105655

Contents lists available at ScienceDirect

Journal of Structural Geology

journal homepage: www.elsevier.com/locate/jsg

Exhumed caldera structures reveal shallow syn-eruptive dyke emplacement in caldera-forming eruptions of Ischia Island

Stefano Vitale [a], Daniele Morgavi [a], Ciro Cucciniello [a], Jacopo Natale [b,*], Thomas Lemaire [a], Mubashir Mehmood [a], Fabrizio Di Fiore [c], Lorenzo Benedetto [d], Sabatino Ciarcia [e]

[a] Dipartimento di Scienze della Terra, dell'Ambiente e delle Risorse, Napoli, Italy
[b] Dipartimento di Scienze della Terra e Geoambientali, Università degli Studi di Bari Aldo Moro, Bari, Italy
[c] Istituto Nazionale di Geofisica e Vulcanologia (INGV), Sezione Roma 1, Rome, Italy
[d] Presidenza del Consiglio dei Ministri-Commissario Straordinario per gli interventi dell'Isola d'Ischia, Napoli, Italy
[e] Dipartimento di Scienze e Tecnologie, Università del Sannio, Benevento, Italy

ARTICLE INFO

Keywords:
Calderas
Ischia Island
Structural geology
Petrography
Volcano-tectonics
Ring dykes

ABSTRACT

Nested structures are a common feature of large calderas, but scientists often infer their existence only through indirect observations, as later eruptive deposits cover the ring-fault zones that bound the different collapsed blocks. The inherent structural complexity of caldera systems makes them challenging to investigate directly. The Island of Ischia (southern Italy) provides a unique opportunity to examine caldera-related structures, such as ring faults and dykes, because block resurgence has uplifted the caldera floor, exhuming its deepest rocks and structures. Due to the dramatic landslide that occurred in 2022 at Casamicciola, a series of previously unobserved dykes hosted in the Mt. Epomeo Green Tuff deposits (MEGT, 62-56.5 ka) were exposed, offering an extraordinary opportunity to study their geometries, intrusion mechanisms, and petrological significance in relation to the dynamics of caldera-forming eruptions. These dykes, located along the northern slope of Mt. Epomeo, situated in the central part of the island, exhibit various shapes, including ball-chained structures, ramp-flat geometries, and orthogonal strands. They are cm-thin and meters long, intruding in the pyroclastic deposits of the intermediate part of MEGT. A notable feature is the presence of a cataclastic shell that encases the cores, composed of fragmented tuff and crystals within a glassy matrix. Petrological and geochemical analyses indicate that the dyke compositions are consistent with those of the Monte Epomeo Green Tuff (MEGT) eruption, thereby linking them to the last phase of the caldera-forming eruption.

Our findings unravel the connections between these dykes and the MEGT eruption, identifying this fault zone as a ring-fault zone of the MEGT caldera and, in turn, providing new insights into the nested caldera structure of Ischia Island and the role of the ring-fault zone during subsequent block resurgence. We propose a model for the origin of the dykes, involving localized volatile-poor injections approaching the surface from a larger feeder dyke that fed the MEGT eruption. These structures, together with the deformation structures identified in the marine deposits beneath the tuff sequence, provide compelling evidence that this area represents a segment of the MEGT caldera ring-fault zone formed during the caldera-forming eruption, and that caldera block-resurgence has been accommodated by the inversion of this ring-fault zone.

1. Introduction

Volcanic calderas are structural depressions formed by the withdrawal of a magma chamber and roof collapse following large explosive or effusive eruptions (e.g., Gudmundsson, 1988; Cole et al., 2005; Martí et al., 2008;Walker, 1984; Kennedy et al., 2018; Cas et al., 2024). Field investigations, analogue and numerical modelling, suggest that caldera depressions are bounded by inward-dipping (normal faults) or outward-dipping (reverse faults), which are called ring-faults. Field investigations, as well as analogue and numerical simulations indicate that

* Corresponding author. Dipartimento di Scienze della Terra e Geoambientali (DiSTEGEO), Università degli Studi di Bari "Aldo Moro", Via Orabona, 4, 70125, Bari, Italy.
E-mail address: jacopo.natale@uniba.it (J. Natale).

https://doi.org/10.1016/j.jsg.2026.105655
Received 16 November 2025; Received in revised form 12 February 2026; Accepted 16 February 2026
Available online 19 February 2026

ring-fault formation is favoured by a stress concentration above the side edges of the shallow magma chamber, implying the occurrence of a precursory minor 'doming' from the larger underlying source reservoir (Gudmundsson, 2007, 2016).

Frequently, large calderas show multiple structural depressions that intersect and/or overlap (e.g., Martí and Gudmundsson, 2000). These intricate volcano-tectonic features, known as "nested" calderas, often originate from a series of high-magnitude explosive eruptions, each contributing to the complex structure (e.g., Cole et al., 2005; Geyer and Martí, 2009). One example is the Campi Flegrei caldera, 12 km in diameter, consisting of at least three main nested rims (Natale et al., 2022, 2024a), formed following the eruption of the Campanian Ignimbrite (39 ka) and reactivated with the Neapolitan Yellow Tuff eruption (15 ka). Another example is the Rabaul caldera in New Britain (Papua New Guinea), which comprises a 14 × 8 km nested caldera formed approximately 200 ka by a series of ignimbrite eruptions that emplaced large volumes of tephra (McKee and Duncan, 2016). Our study focuses on another nested caldera, Ischia Island (southern Italy), which also features complex block-resurgence. In this work we conducted a multidisciplinary investigation of a portion of the Island of Ischia, which is dominated by a large caldera infilled with the Monte Epomeo Green Tuff sequence (MEGT; 62–56.5 ka) and subsequent volcanic deposits interlayered with marine and continental sediments.

We integrate structural and petrological data on magmatic dykes intruding the MEGT deposits on the northern slope of the resurgent block (Mt. Epomeo) in the central area of the island (Fig. 1). The aim of this work is to characterise these dykes in terms of geometries, emplacement mechanisms and to understand the petrological link to caldera-forming eruptions in the framework of the overall caldera evolution. In particular, we aim to investigate the relationships between

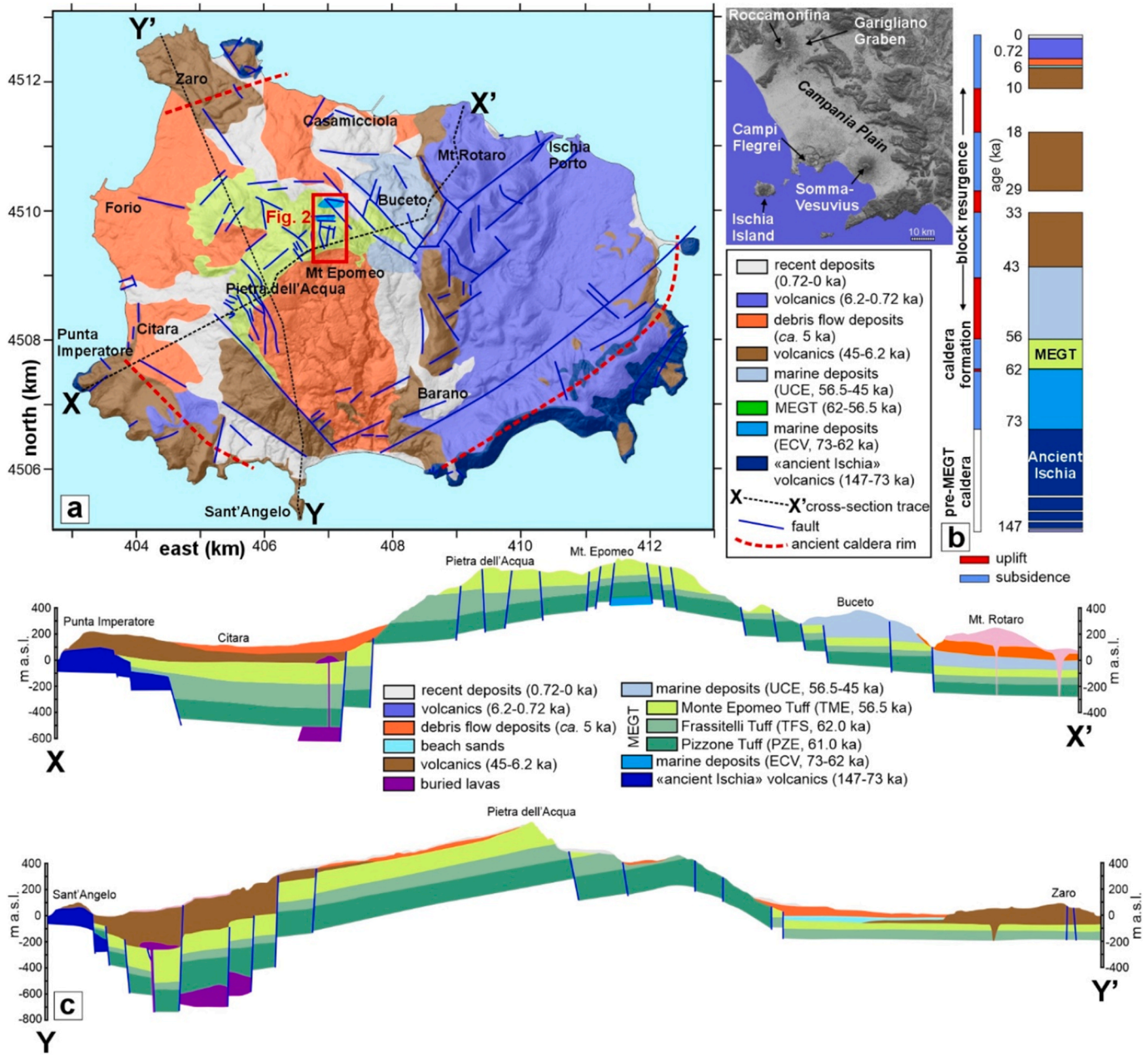

Fig. 1. (a) Schematic geological map of Ischia Island (modified after Vitale et al., 2025); (b) stratigraphic log; (c) Simplified geological cross-section of the Ischia Island (modified after Vitale et al., 2025). MEGT: Monte Epomeo Green Tuff. (For interpretation of the references to colour in this figure legend, the reader is referred to the Web version of this article.)

these structural elements and the MEGT eruption, thereby providing additional evidence for a nested caldera structure and the reactivation of its ring-fault zone during the block resurgence.

2. Geological setting

The Quaternary tectonic history of the Tyrrhenian margin of the southern Apennine orogenic chain in southern Italy (Campania region) is characterised by extensional events that have formed coastal plains, such as the Garigliano Graben and the Campanian Plain (Fig. 1a; e.g., Ciarcia and Vitale, 2025). Closely related to these tectonic events, volcanism occurred, forming the Roccamonfina volcano in the north (e.g., Natale et al., 2023, 2026 and references therein), the Ischia Island (e.g., Sbrana et al., 2020; and references therein), the Campi Flegrei caldera (Orsi, 2022 and references therein) and the Somma-Vesuvius volcano (Guarino et al., 2024 and references therein) to the south. Roccamonfina and Somma-Vesuvius are both defined by a central volcano structure and a summit caldera, whereas large caldera volcanic fields characterise Ischia Island and Campi Flegrei.

The caldera of Ischia Island (de Vita et al., 2010; Sbrana et al., 2009, 2020; Vezzoli et al., 2009) is characterised by an elliptical shape, with an external rim of 9.0 x 6.4 km. Outside the rim, the oldest rocks, with ages ranging from 147 to 73 ka, are exposed; in contrast, the caldera is filled by the Monte Epomeo Green Tuff sequence (MEGT; 62-56.5 ka), with a resurgent block broadly in the centre (Mt. Epomeo; Fig. 1a), and younger volcanic deposits, interspersed with marine and continental sediments.

In particular, the oldest rocks within the caldera are marine/lacustrine deposits of the Cava Celario unit (ECV; ISPRA, 2018; Vitale et al., 2025), which underlie the thick pyroclastic succession of the MEGT sequence (Fig. 1c), with an age spanning between 62 and 56.5 ka (ISPRA, 2018; Sbrana et al., 2018). The latter succession consists of three units: Pizzone Tuff (PZE), Frassitelli Tuff (TFS), and Monte Epomeo Tuff (TME). In the central part of the caldera, these rocks are covered by post-caldera marine to continental deposits of Buceto Syntheme (UCE; Fig. 1). Synchronously with marine deposition, the central sector of the caldera underwent uplift, and, starting at 43 ka, the Mt. Epomeo block resurgence occurred, alternating between uplift and subsidence phases over time (Carlino, 2012, 2022; Vitale et al., 2025). During subsidence periods, volcanism occurred around the resurgent block (Acocella and Funiciello, 1999; Carlino, 2012, 2022). Furthermore, the uplift triggered several debris flows and avalanches along the mountain slopes, travelling for tens of kilometres underwater as turbidite currents (de Della Seta et al., 2012; Sbrana et al., 2018). The Arso lava flow was the last eruption to occur in historical times (1302 CE; Iovine et al., 2017). In recent years, Ischia has been affected by shallow seismicity, including the August 21, 2017 earthquake (Mw 4.0 ± 0.3), which caused extensive damage and fatalities in the town of Casamicciola (e.g., De Novellis et al., 2018). This seismicity is associated with hydrothermal activity and the subsidence of Mt. Epomeo (Manzo et al., 2006; Galvani et al., 2021), which has activated faults on the northern slope of the resurgent block (Silva-Fragoso et al., 2024).

Recently, Vitale et al. (2025) investigated the deformation structures hosted in the marine deposits underlying the MEGT sequence, suggesting a close relationship between these structures and the formation of the MEGT caldera. According to these authors, the area was the location

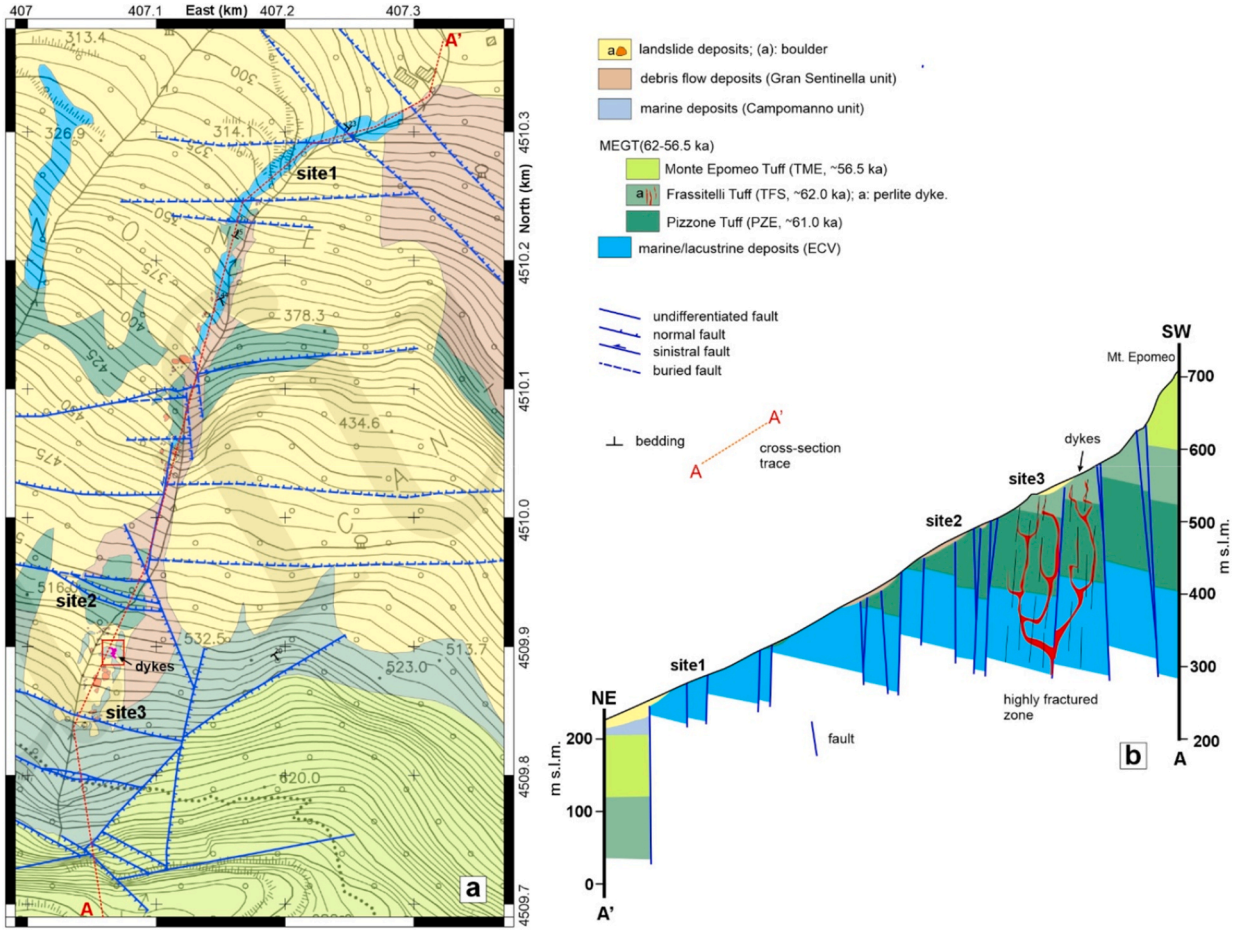

Fig. 2. (a) Geological map of the Cava Celario (UTM projection, WGS84 33N); (b) NE-SW oriented geological cross-section. The thicknesses of dykes were exaggerated.

of a major ring-fault zone exhibiting a nested caldera geometry, with a depocenter in the southwest sector of the ancient caldera (pre-MEGT). The Authors also hypothesised that ring-faults were subsequently reactivated and inverted, accommodating the uplift of the Mt. Epomeo block, located in the centre of the island.

3. Materials and methods

We analysed the Cava Celario engraving located along the northern slope of Mt. Epomeo (Fig. 2). This area was exposed following the dramatic landslide on November 26, 2022, triggered by several days of intense rainfall (Romeo et al., 2023), which caused 12 fatalities. We performed stratigraphic and structural surveys, collecting measurements of attitudes of dyke boundaries, faults and fractures. The mapping of the area was performed using the Qfield app on "Tablet A″ Samsung tablet. The final map was created using the free QGIS software.

3.1. Field and drone structural data

We measured the plane attitudes of faults, fractures and dyke boundaries. Occasionally, faults exhibit kinematic indicators, such as slickenside striations and fibres. Kinematics was evaluated, where possible, using slickensides or Riedel shears. Structural data were analysed using the free software TectonicsFP (https://github.com/freiter/TectonicsFP). Structural data are presented in stereographic projections and rose diagrams.

To analyze the spatial distribution of dykes and the main deformation structures and to overcome the limitations posed by articulated topography, we conducted an Unmanned Aerial Vehicle (UAV) survey in March 2023. We provided a high-resolution Virtual Outcrop Model, collecting ~550 photographs with a DJI Mavic Air 2 mounting a stabilised 0.5" CMOS 12 MP sensor and a 24 mm-equivalent focal length and a 4:3 aspect ratio in its best acquisition mode which has consistently provided excellent results in previous applications (e.g., Diamanti et al., 2022; Natale et al., 2024a, 2026). The orthomosaic has a maximum resolution of approximately 1 cm/pixel.

To perform petrographic analysis, we collected several representative samples from the dykes, from which 10 thin sections were prepared using standard techniques. Petrographic observations were made in plane-polarised and cross-polarised light using a Nikon Eclipse e200 microscope, and microphotographs were taken with a Zeiss Axiocam 2008 color camera connected to the microscope.

3.2. X-ray fluorescence data

Samples were also analysed to gather geochemical data. Small chips from the samples were cleaned in an ultrasonic bath and ground to a grain size of less than 75 μm using a Retsch PM-100 planetary mill with agate grinding balls at the Department of Earth, Environment and Resource Sciences (DiSTAR, University of Naples Federico II). Four grams of rock powder were used to prepare pressed powder pellets. The powder, mixed with 1 ml of Polyvinyl alcohol solution, was pressed at 20 tons for 20 s. The bulk-rock compositional data were determined using pressed powder pellets with an Axios Panalytical X-ray fluorescence (XRF) spectrometer, equipped with six analyser crystals, three primary collimators, and two detectors (flow counter and scintillator), operating at different kV and mA settings for each analyte. Analytical uncertainties are in the order of 1–2% for major elements and 5–10% for trace elements. Further details are reported in Cucciniello et al. (2023).

3.3. Scanning electron microscopy data

Approximately 300 mineral and glass compositions (Supplementary Table S1) were obtained at the DiSTAR by an Oxford Instruments Microanalysis Unit and a JEOL JSM-5310 Energy Dispersive Spectrometry (EDS) microscope (operating at 15 kV primary beam voltage, 50-100 μA filament current, 20 mm working distance and 50s net acquisition time). The following standards were used for calibration: diopside (Mg), wollastonite (Ca), anorthoclase (Al, Si), albite (Na), rutile (Ti), almandine (Fe), Cr_2O_3 (Cr), rhodonite (Mn), orthoclase (K), apatite (P), fluorite (F), barite (Ba), strontianite (Sr), Smithsonian orthophosphates (REE, Y), pure niobium (Nb), pure vanadium (V), pure nickel (Ni), zircon (Zr, Hf), Corning glass (Th and U), sphalerite (S), sodium chloride (Cl). Backscattered electron (BSE) images were obtained with the same instrument. The measured and certified analyses of international standards for the SEM-EDS analyses are reported in the Supplementary Table.

3.4. Electron probe micro-analyser analysis

Major element compositions on the samples were determined by an electron probe micro-analyser (EPMA) JEOL JXA-8200 equipped with five wavelength dispersive spectrometers (WDS) and installed at the High-Pressure High Temperature (HPHT) Laboratory of Experimental Volcanology and Geophysics of the Istituto Nazionale di Geofisica e Vulcanologia (INGV, Rome, Italy). Analyses were performed on carbon-coated thin sections under high-vacuum conditions using an accelerating voltage of 15 kV, an electron beam current of 7.5 nA, and a beam diameter of 2.5 μm. Elemental counting times were 10 s on the peak and 5 s on each of two background positions, except for chromium, which was measured for 20 s on the peak and 10 s on each background position. Corrections for inter-elemental effects were made using a ZAF (Z: atomic number; A: absorption; F: fluorescence) procedure. Calibration used a range of standards from Micro-Analysis Consultants (MAC; http://www.macstandards.co.uk): albite (Si-PET, Al-TAP, Na-TAP), forsterite (Mg-TAP), augite (Fe-LIF), apatite (Ca-PET), orthoclase (K-PET), rutile (Ti-PET), rhodonite (Mn-LIF) and JEOL Cr metal (Cr-PET). MINERAL from the MAC standards was used as the quality-monitoring standard and for calculating accuracy and precision. Accuracy was better than 1-5% except for elements with abundances below 1 wt%, for which accuracy was better than 5-10%; the precision was typically better than 1-5% for all analysed elements (Di Fiore et al., 2021; Mollo et al., 2024).

3.5. Estimation of intensive parameters

Temperature conditions of crystallisation of the dykes were determined based on plagioclase-alkali feldspar and alkali feldspar-liquid equilibria using the method of Putirka (2008). Water contents in the dykes were estimated using the K-feldspar–liquid hygrometer developed by Mollo et al. (2015) and the plagioclase-liquid hygrometer developed by Masotta and Mollo (2019). Pressure estimates were derived from the clinopyroxene composition of Nimis (1999).

4. Results

4.1. Geological map, cross-section and VOM

Fig. 2a shows the geological map of the Cava Celario, realised in April-July 2023. The general stratigraphic architecture is characterised by the superposition of the MEGT pyroclastic succession, composed of PZE, TFS, and TME units, onto the ECV deposits. The entire succession is, in turn, covered by debris flow deposits of Gran Sentinella (GST) and, finally, by recent landslide and colluvial sediments. The structure of the northern slope of Mt. Epomeo consists of a homoclinal dipping to the south of 20-30° (Fig. 2b). The marine-continental succession is cut by high-angle faults, mostly dipping to the north and with dominant normal kinematics and displacements from a few centimetres to some meters. We reconstructed a VOM of the northern sector of the Cava Celario and extracted the orthomosaic shown in Fig. 3a. One of the areas with a high concentration of dyke is shown in the zoomed orthomosaics (Fig. 3b and c), where some dyke segments are present. We extracted the azimuths of

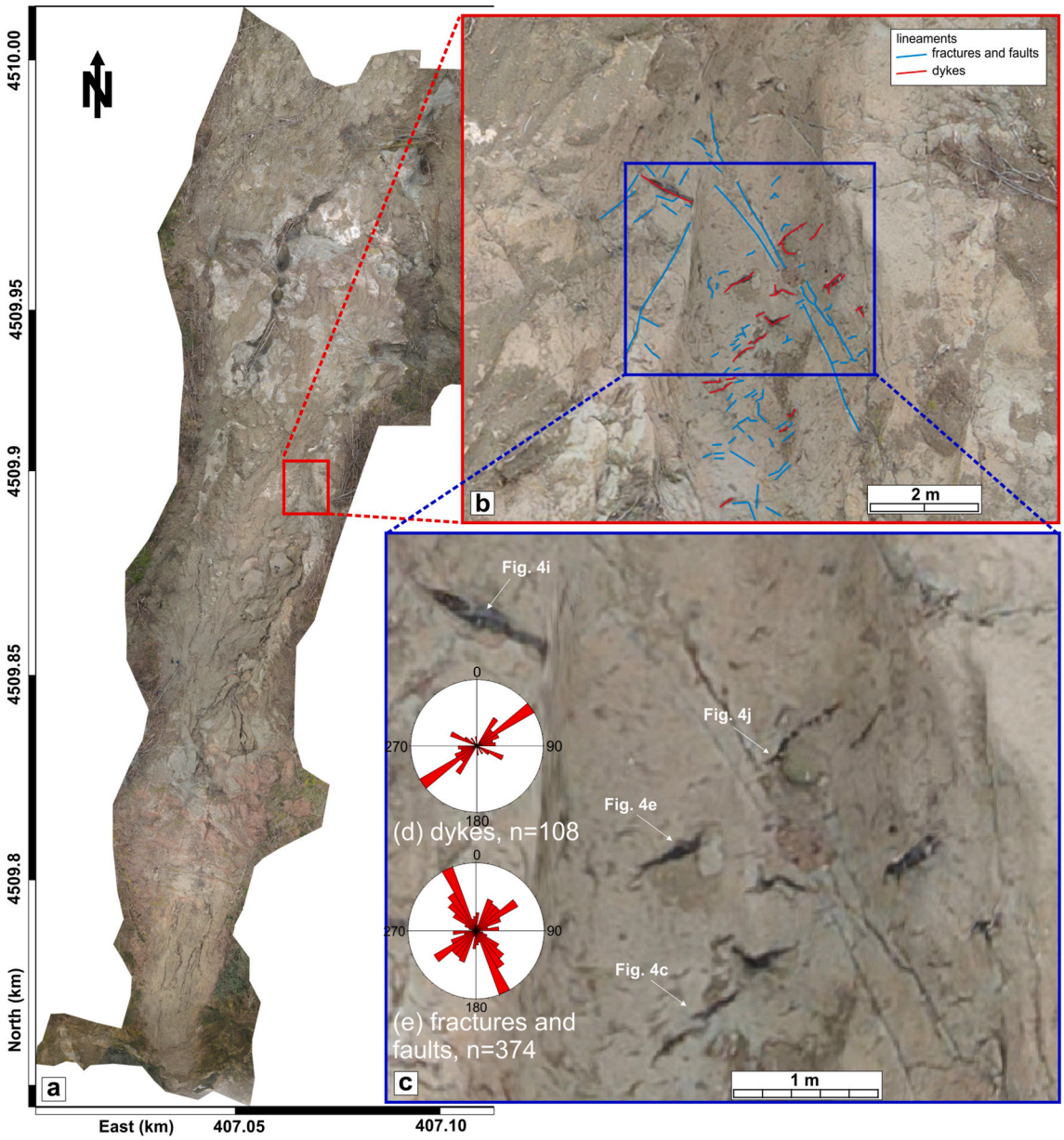

Fig. 3. (a) VOM of the upper part of Cava Celario (UTM projection, WGS84 33N); (b) Zoomed area showing the analysed fracture, faults and dyke lineaments; (c) Close-up view of some dykes. Rose-diagrams of (d) dykes and (e) fractures and faults.

the dyke and fracture lineaments from the zoomed area. To obtain a weighted statistical distribution of dykes and fractures, we divided them into equal-length segments. Fractures and fault lineaments were selected near the dykes. The rose diagrams of dykes (Fig. 3d) indicate a dominant NE-SW strike similar to the secondary direction of fractures and faults (Fig. 3e) that are dominated by a NNW-SSE direction.

4.2. Mesoscale structures

4.2.1. Dykes

We analysed in detail site 3 (Fig. 2), characterised by a large exposure of the Frassitelli Tuff (TFS) and hosting some magmatic dyke segments. The host rock is characterised by weak layering (Fig. 4a–c, h, i). Dykes are frequently formed by single lens-shaped structures with a dark core composed of perlitized obsidian and a reddish halo (Fig. 4a–f) consisting of cataclasite with a glassy matrix. In other cases, dykes show a ramp-flat geometry, with flats parallel and ramps orthogonal to the tuff layering (Fig. 4b). Lens-shaped dykes generally form parallel sets (Fig. 4c). The dyke margin shape is irregular, and some dykes show tubular apophyses (Fig. 4g). Frequently dykes display a ball-chained structure made by larger segments connected by thinner strands (Fig. 4e). The dyke tips are rounded (blunt tips) as well as the cataclastic zones (Fig. 4d). The thicknesses of the dykes and cataclastic zone are normally lesser than 20 cm and 5 cm, respectively. We measured the thickness variation for three lens-shaped dykes (Fig. 5a–c). Results indicate that the thicknesses of dyke cores and cataclastic zones vary, showing a flatted shape with some highs and lows corresponding to enlargements and narrowing. Finally, we measured the attitudes of the dyke boundaries. The stereographic projection (Fig. 5d) indicates that the dykes are frequently subvertical and form three major sets. This is highlighted by the rose diagram (Fig. 6e), marking a major ENE-WSW/E-W set and a secondary N-S set.

4.2.2. Faults and fractures

In the Cava Celario area (Fig. 2a), several main and secondary faults are exposed, generally characterised by E-W and NW-SE directions with

Fig. 4. Pictures of mesoscale exposure of the dyke swarm: (a) lens of a dyke segment with a maximum thickness of 18 cm formed by a core surrounded by a cataclastic envelope; (b) ramp-flat geometry; (c) lenses of dyke segments; (d) zoomed dyke tip; (e) thin apophysis branching from a ball structure; (f) close-up view of a dyke segment boundary; (g) circular section of a thin apophysis; (h) vertical dyke with a thickness increase in the centre (ball-chained structure); (i) 2 m long vertical dyke; (j) segmented dyke; (k) ameboid-shaped dyke.

dominant normal kinematics and secondarily by ca. N-S faults. Near the dykes (site 3), several nearly vertical normal faults are exposed, crosscutting the TFS, whose displacement is marked by dislocated green tuff *fiamme* (Fig. 6a). At lower topographic elevations, a WNW-ESE-directed fault, crosscutting the PZE, is associated with intense hydrothermal mineralisation along the fault plane (Fig. 6b and c). This fault, characterised by ca. 10 m of displacement, exhibits a dominant normal kinematics based on stratigraphic evidence. Fractures in site 3 indicate E-W, ENE-WSW, NW-SE, and N-S preferred directions (see the stereographic projection in Fig. 6b). Again, within PZE, an NW-SE fault dipping to SW (Fig. 6d) shows striations and steps indicating oblique kinematics with normal and right-lateral components. Additionally, NNE-SSW-directed, left-lateral reverse faults are present in PZE (Fig. 6e) and exhibit striations and steps. E-W/WNW-ESE-striking normal faults are also present (site 2; Fig. 6f), dislocating the stratigraphic transition between PZE and the underlying marine sediments (ECV). Finally, in site 1, E-W-striking faults are cut by a NW-SE-directed fault. This structure is almost vertical, with approximately 1 m of displacement within the ECV, resulting in a

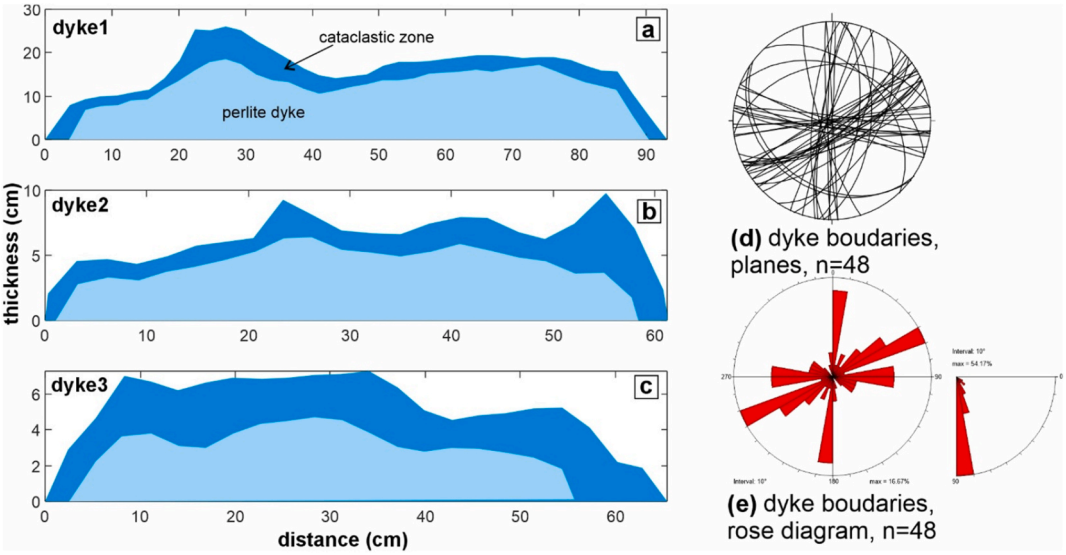

Fig. 5. Thickness of perlitized dykes and alteration halo (a) dyke1 in Fig. 4a; (b) dyke2 in Fig. 4c; (c) dyke3 in Fig. 4c. (d) Stereographic projections (lower hemisphere, Schmidt net) and (d) rose-diagrams of direction and dip angle of dyke margins.

lowering of the NE sector. However, the fault plane shows segments dipping to the NE and to the SW, with reverse and normal kinematics, respectively.

4.3. Dyke structure

To examine the internal structure of the dyke and its contact with the host tuff, we collected a representative sample and prepared a polished slab (Fig. 7a). The whole structure consist in three homogeneous parts: (1) a dark central part (dyke core) composed of hydrated glass with a perlite structure that has a thickness of 2-3 cm with relicts of phenocrysts, (2) a cataclastic zone surrounding the dyke with a patchy pattern with a thickness of 1-2 cm and (3) the host rock corresponding to a yellow tuff (TFS) with a brown alteration at the boundary with the cataclastic zone.

4.3.1. Dyke core

The analysed thin sections of the central part of the dyke (core) show a homogeneous perlite structure. It consists of spheroids and ellipsoids of glass embedded by an intricate array of major anastomosing and crosscutting cracks and minor concentric fractures enveloping the spheric grains (Fig. 8a and b). The largest grains have a diameter of 2 mm. However, most of them are less than 1 mm in diameter. Some phenocrysts of sanidine and mica are present (Fig. 8a). The back-scattered electron images show that the dyke core exhibits a patchy pattern, with some parts of the glass completely transformed, hydrated, and perlitized, characterised by circular and shaded boundaries (Fig. 8c and d). Sanidine and mica crystals always show fractures.

4.3.2. Cataclastic zone

The cataclastic zone forms a shell around the dyke core. It comprises fragments of sanidine, clinopyroxene, and mica crystals, embedded in a glassy matrix (Fig. 7b–d, 8e-h). Generally, sanidine fragments show a preferred orientation parallel to the dyke boundaries (Fig. 7b–d), depicting a fluidal fabric. At the transition with the perlitized dyke, the structure is defined by phenocrysts embedded in hydrated glass, which in turn is enveloped by glass with a perlite structure (Fig. 8c and d). The hydrated glass, in contact with the phenocrysts, forms cuspid and lobe-shaped laminations (Fig. 8e and f). The general texture resembles cataclasite, with large crystals crushed (Fig. 7b and 8g) and layers of fine cataclasite (Fig. 7b, c, 8h) showing rounded clasts.

4.3.3. Host rock

The host rock is a massive lapilli tuff with large crystals of sanidine, mica, and clinopyroxene (Fig. 7b–d) embedded in a lithified coarse ash and lapilli matrix. The boundary between the host rock and the cataclastic zone is irregular rather than sharp. The tuff close to the cataclastic zone shows an altered halo characterised by a darker colour compared to the unaltered tuff.

4.4. Classification and petrography

The dykes are vitrophyric, with phenocrysts and microphenocrysts of sanidine, plagioclase, clinopyroxene, mica, opaque oxides, and apatite microlites, set in a vitreous matrix with perlitic cracks. Sanidine phenocrysts have a wide range of compositions (Or_{53-92}). The concentrations of Sr and Ba in the sanidine are low (Supplementary Table S1), consistent with the low Sr and Ba levels in the host rocks (MEGT). Plagioclase phenocrysts and microphenocrysts range from bytownite to andesine (An_{36-83}). The feldspar analyses extend well beyond the range of the analysed feldspars in the MEGT rocks (D'Antonio et al., 2021, Fig. 9a). Clinopyroxene is diopside ($Ca_{47-49}Mg_{34-40}Fe_{13-18}$; Mg# = 66-76, where $Mg\# = Mg*100/(Mg + Fe_t)$). TiO_2 and Al_2O_3 are generally low (Supplementary Table S1). Clinopyroxene compositions plot (Fig. 9b) within the field defined by Mg-rich clinopyroxenes of MEGT (D'Antonio et al., 2021) and other Ischia rocks (Melluso et al., 2014). Opaque oxides are titaniferous magnetites. The chemical composition of titaniferous magnetite is broadly constant in the dykes (ulvöspinel component = 20-22 mol%). Mica is a Mg-rich (MgO = 13.96-16.27 wt %) phlogopite with a TiO_2 content rather constant (5-5.74 wt%). Apatite typically occurs as microlites in the groundmass or as inclusions in the feldspar or clinopyroxene grains. It has high F (1.70-2.60 wt%) and low light rare earth element (LREE) concentrations.

4.5. Geochemistry

Major and trace element compositions of the dyke cores are reported in the Supplementary Table S1. Hand specimen and petrographic observations indicate an alteration of the dykes, showing that late or post-crystallisation fluid-rock interactions may have modified their compositions. We, therefore, did not use whole-rock major element data but only alteration-resistant elements (e.g., Ti, Zr, Nb, Y) and their ratios for geochemistry-based modelling and interpretation.

Based on petrography, chemical classification (total alkali silica,

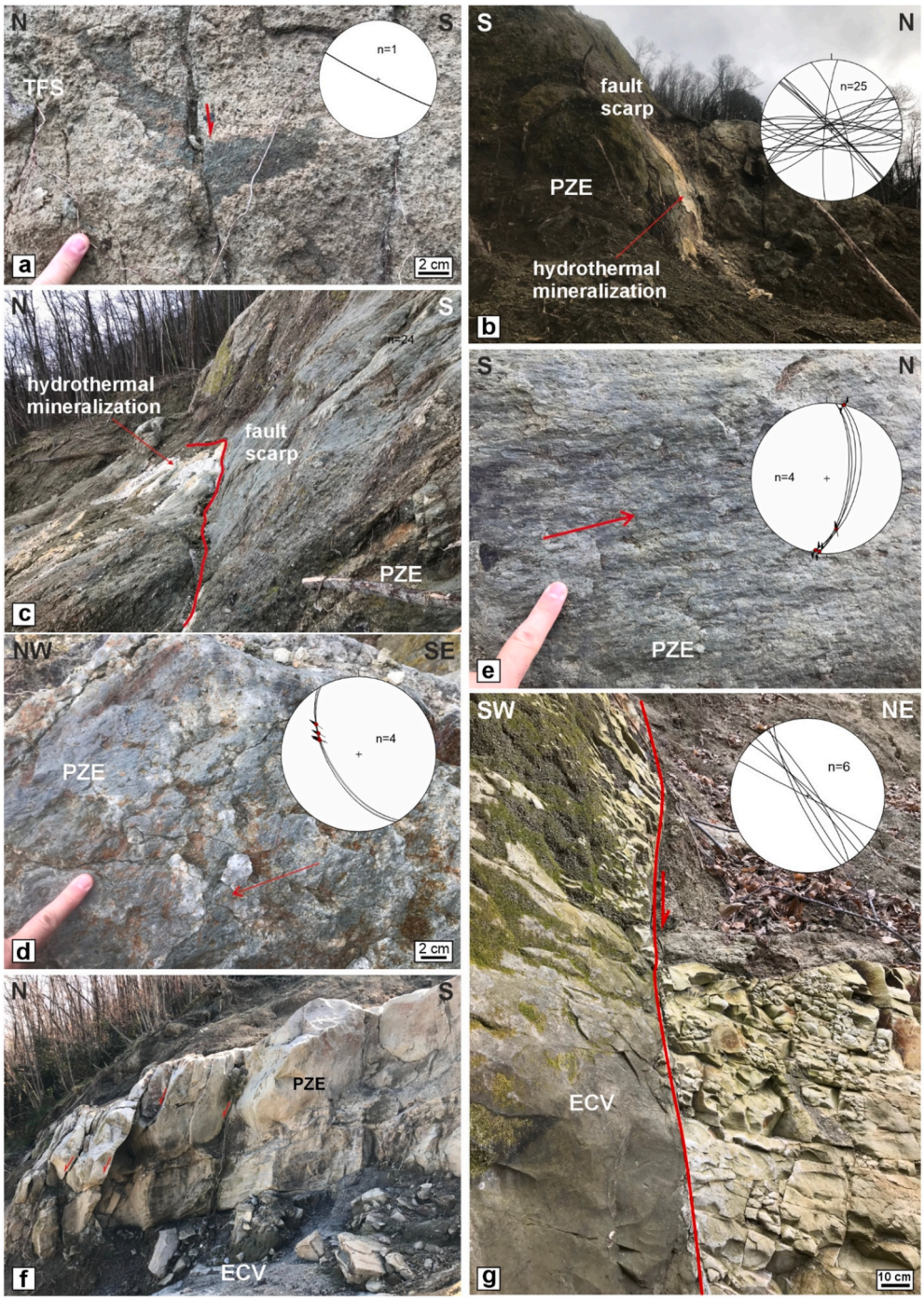

Fig. 6. Examples of mesoscale faults along the Cava Celario engraving. (a) High-angle normal fault in TFS (site 3) and stereographic projection of fault plane; (b, c) Main E-W normal fault in PZE (site 3) and stereographic projection of fracture planes in the site; (d) NW-SE oblique fault showing striations (site 3) and stereographic projection of fault plane with slip vectors; (e) NNE-SSW left-lateral fault with striations and steps (site 3), and stereographic projection of fault plane with slip vectors; (f) E-W normal faults dipping northward with minor displacement at the passage between PZE and ECV (site 2); (g) Sub-vertical main dip-slip fault with metric displacement (site 1) and stereographic projection of fault planes.

TAS, Le Maitre, 2002, Fig. 9c; K_2O vs SiO_2, Peccerillo and Taylor, 1976, Fig. 9d) and CIPW norms, the dykes (whole rocks and glasses) are classified as trachytes and trachyphonolites. Several samples of glasses reach full peralkaline conditions [P.I., peralkaline index, molar (Na + K)/Al > 1]. The glasses are chemically uniform with SiO_2 in the range 61.10-63.17 wt%, TiO_2 0.36-0.58 wt%, Al_2O_3 18.31-19.11 wt%, FeO_t 2.15-4.12 wt%. All samples contain low MgO contents (0.24-0.55 wt%). The alteration-resistant trace elements (in the whole-rock) also have narrow ranges of concentration (e.g., Zr = 242-323 ppm, Nb = 33-43 ppm, Y = 32-47 ppm) and ratios of concentrations (e.g., Zr/Nb = 7-9, Y/Nb = 0.8-1.3). These element values and ratios are consistent with those of MEGT (Brown et al., 2008, 2014) and other volcanic products from Ischia (Melluso et al., 2014; Casalini et al., 2017, and references therein).

4.6. Crystallisation temperature and water content estimations

The estimated crystallisation temperature using the alkali felspar-

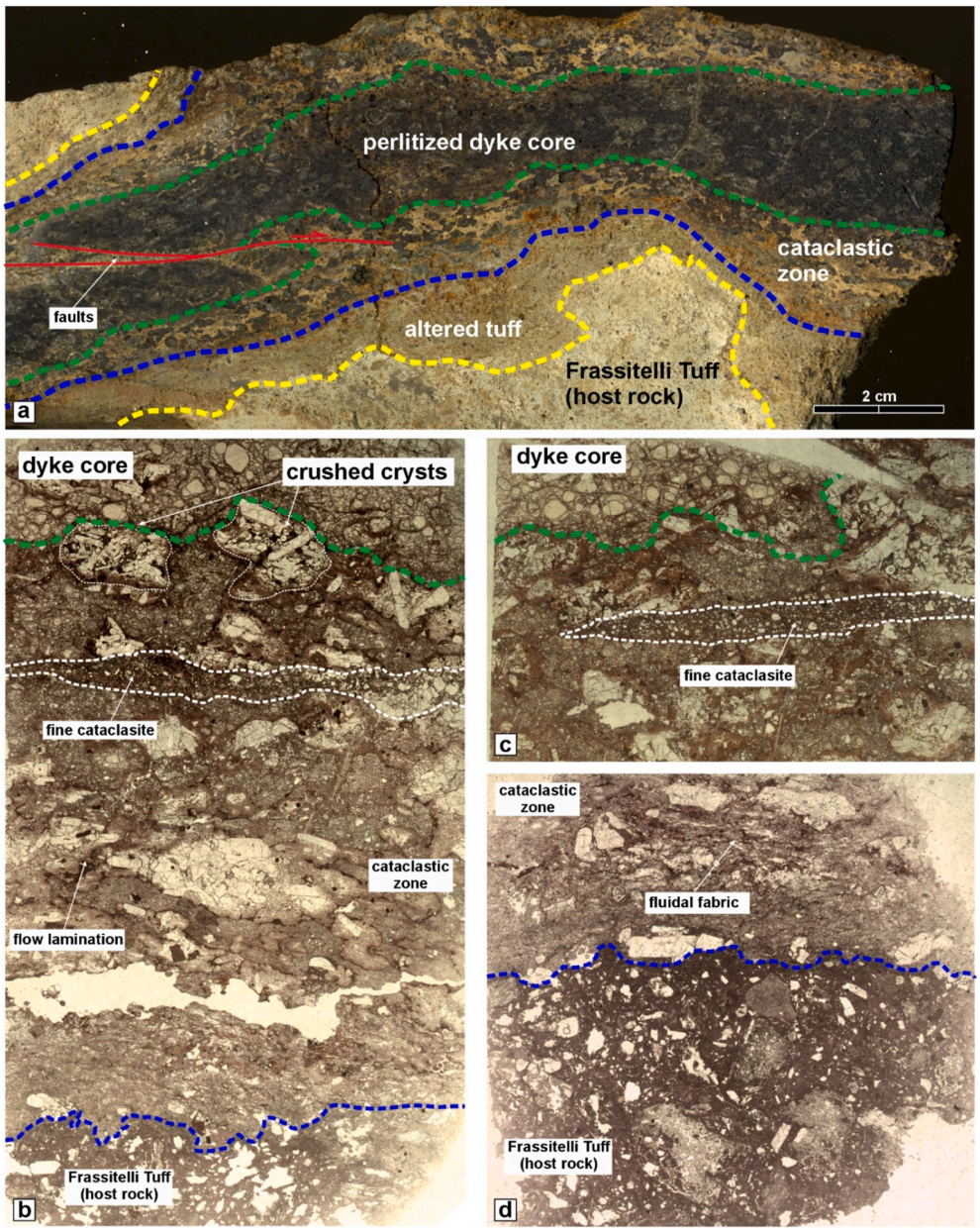

Fig. 7. (a) Slab of a dyke hosted in the TFS; (b-d) microphotographs of the transition from the host rock to the cataclastic zone and the perlitized dyke.

liquid equilibria and plagioclase-alkali feldspar equilibria (see methods) is 889 ± 47 °C. The negative values of the clinopyroxene barometer and the low or absent ^{VI}Al (Supplementary Table S1) in the clinopyroxenes suggest low crystallisation pressures. The water content in the perlitized dykes is approximately 5 wt%. (see methods).

5. Discussion

5.1. Mesoscale structures

The stereographic projection of dyke boundaries (Fig. 5d and e) indicates that they are predominantly steeply dipping, with some segments showing gentle dips. Dyke strands show a main preferred direction of about ENE-WSW and secondary directions of E-W and N-S. The ENE-WSW direction is well-fit with the dominant lineament direction of the dyke and secondary direction of fracture mapped on the VOM (Fig. 3d and e). The dominant NNW-SSE of fracture and fault lineaments is associated with the major NNW-SSE-directed structures that crosscut the whole outcrop (Fig. 3b and c). According to field observations (e.g., Greiner et al., 2023) and numerical models (e.g., Gudmundsson, 2022), fluid-driven fractures may follow pre-existing faults or fractures along their paths, particularly when these structures are steeply dipping and have negligible tensile strength. It follows that we can suppose that the magma intruded along pre-existing faults and fractures, which likely formed during the initial stages of caldera formation.

Furthermore, the evidence that some dykes are formed by different vertical straight segments that are also orthogonal between them strengthens the idea that some dykes used pre-existing vertical fractures that generally form orthogonal sets (e.g., Caputo, 1995, Fig. 11a). It follows that the host rock (Frassitelli Tuff) was lithified when the dykes intruded. Accordingly, the presence of cataclasite surrounding the dyke core indicates that the host tuff deformed under brittle conditions.

The lens geometry of several dyke segments along a vertical section indicates that the magma flow was both vertical and horizontal (e.g., Allgood et al., 2025). The coexistence of horizontal and vertical flow, frequently observed in volcanic environments (e.g., Allgood et al., 2025;

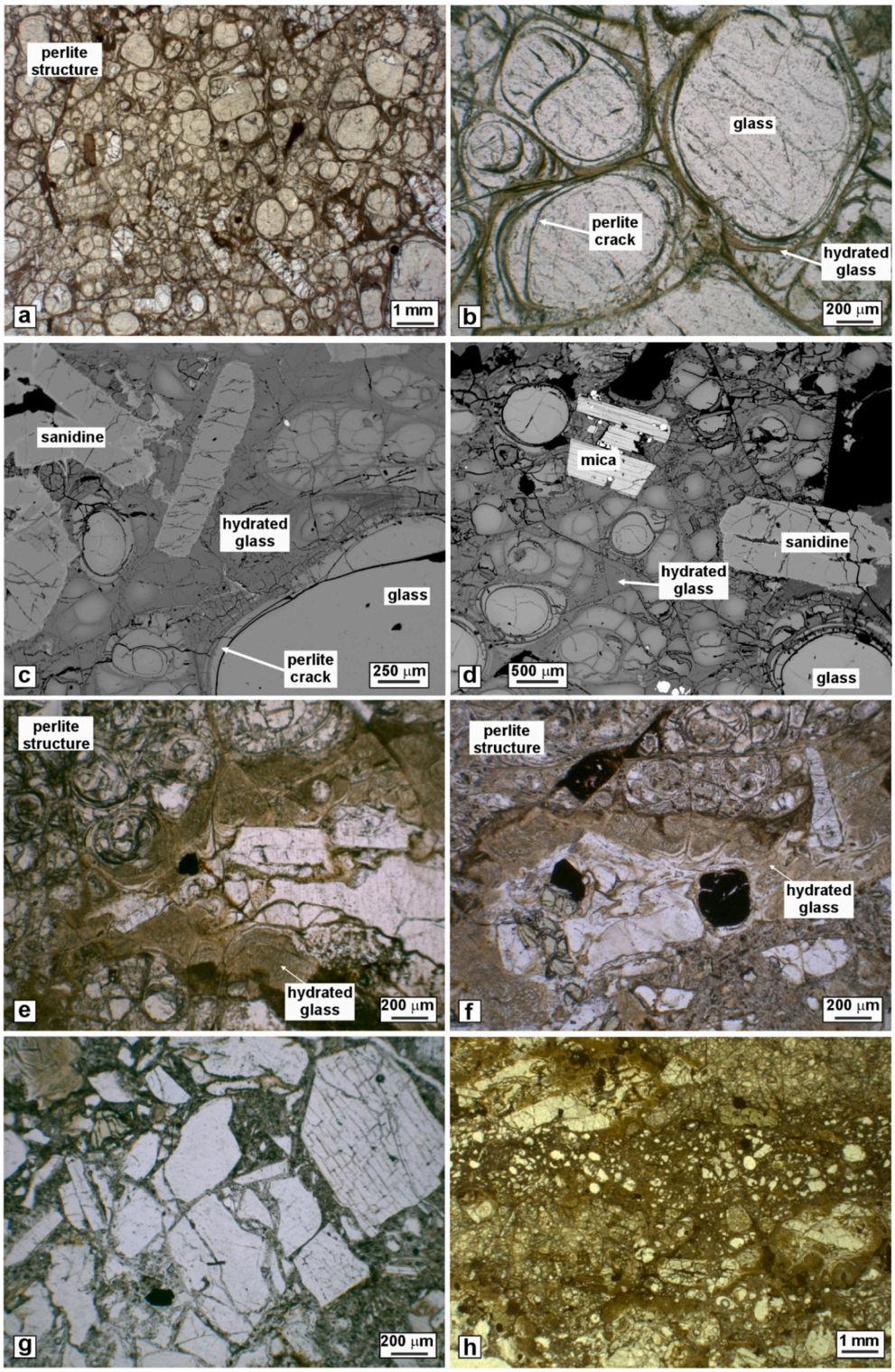

Fig. 8. (a, b) Perlite structure (perlitized dyke) as observed under optical microscope; (c, d) Perlitized dyke as observed under Scanning Electron Microscopy; (e, f) Transition between perlitized dyke and cataclastic zone (optical microscope); (g) Crushed feldspar and clinopyroxene crystals (optical microscope); (h) Fine cataclasite (optical microscope).

Hobé et al., 2025), reflects magma propagation with combined vertical and lateral components. This feature is common when magma is approaching the ground surface (e.g., Tramparulo et al., 2018), where the principal (lithostatic) stress σ1 is very low and nearly vertical, a feature consistent with caldera collapse formation (e.g., Diamanti et al., 2022; Natale et al., 2024a,b).

The presence of ball-chained dykes (Fig. 11a) can be attributed to a different causes, including: (i) dyke interaction with rocks with different strengths/stiffness (Gudmundsson, 1984); (ii) in the intersection between dyke and faults (Galindo and Gudmundsson, 2012); (iii) localized differences in dyke overpressure, for example, if magma pressure oscillates (e.g., due to supply pulses or viscosity contrasts), the intrusion

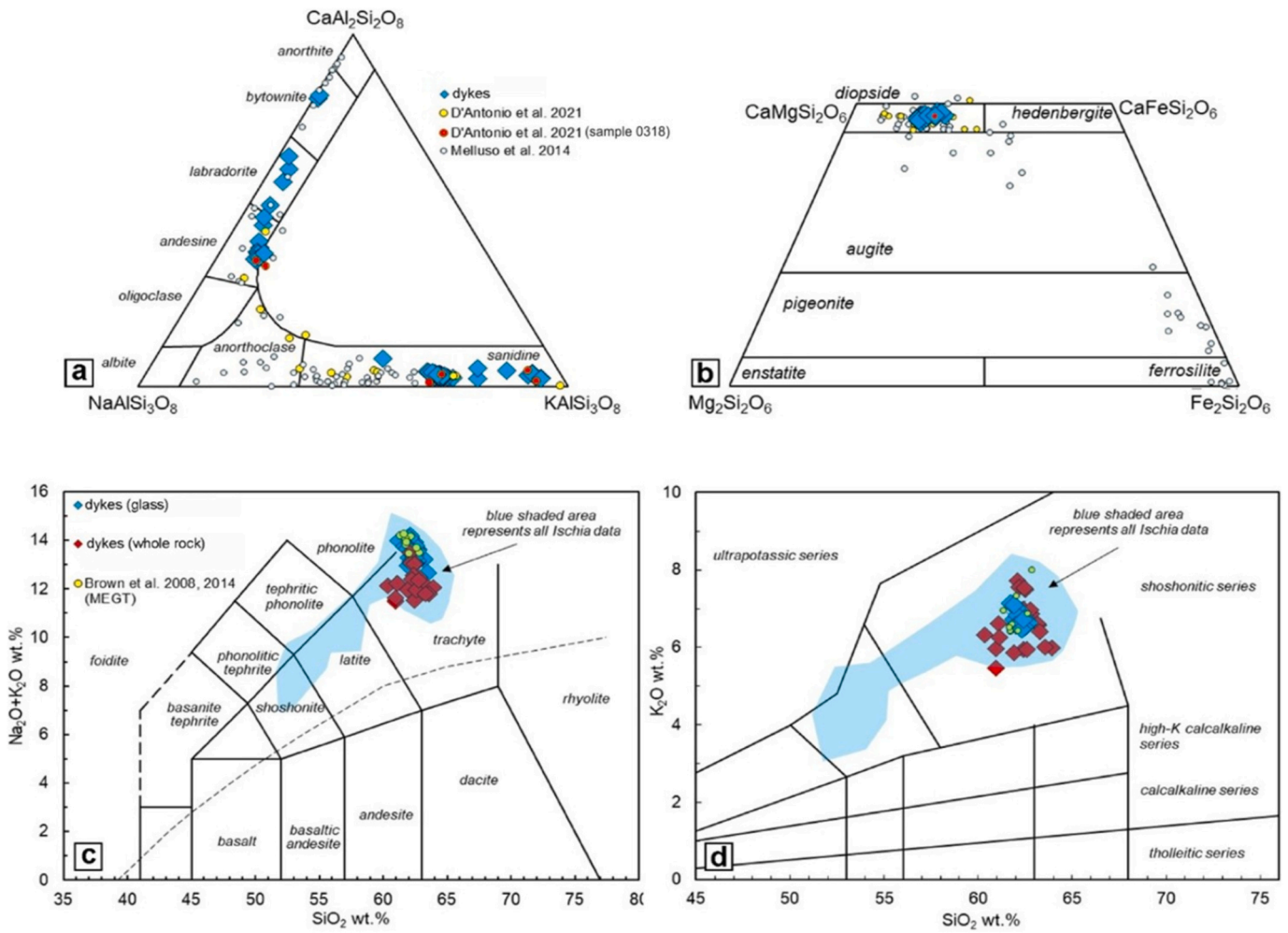

Fig. 9. Perlitized dyke composition: (a) feldspar compositions, small circles are literature data (D'Antonio et al., 2021; Melluso et al., 2014); (b) pyroxene compositions in the Ca–Mg–Fe quadrilateral, small circles are literature data (D'Antonio et al., 2021; Melluso et al., 2014); (c) total Alkali vs. SiO_2 (TAS; Le Maitre, 2002) and (d) K_2O vs. SiO_2 (Peccerillo and Taylor, 1976) classification diagrams, literature data sources: Casalini et al., (2017) and references therein; Melluso et al., (2014); Brown et al. (2008, 2014). (For interpretation of the references to colour in this figure legend, the reader is referred to the Web version of this article.)

may inflate episodically, creating discrete magma batches along the same fracture. However, the ball-chained geometry, combined with the presence of dykes with ramp-flat (Fig. 11b) or ameboid geometries, suggests that sub-horizontal planar anisotropies in the host rock, such as the tuff layering, and pre-existing fractures and faults, have played a significant role in their formation.

In general, mechanical layering can strongly affect the dyke-path geometry and the conditions for dyke-path arrest. It depends on the properties of the host rock, including lithology, texture, and physical properties such as stiffness (Gudmundsson, 2020, 2022). However, in the case of the studied dykes, the tuff is lithologically homogeneous, characterized by a discontinuous layering. In such a scenario, only locally is the layering capable of deviating the dyke trajectories or of forming ball-chained structures.

The exposed dykes are hosted in TFS rather than in the overlying TME, implying they formed during the first phases of the TME eruption, possibly as part of a precursory ring-dyke injection episode preceding caldera collapse. This is strengthened by the occurrence that some dykes are dismembered, likely due to the last phase of the caldera formation synchronous with the TME eruptive event (56.5 ka).

The structural survey of faults and fractures reveals a diverse range of structures, including high-angle normal and reverse faults with E-W and NW-SE directions, with the latter structures crosscutting the former. Faults show displacements varying from a few centimetres to tens of meters. A few strike-slip faults are present, which can be explained as transfer structures between fault strands rather than regional tectonic faults, similarly to faults occurring along radial planes in the Somma-Vesuvius volcano associated with the summit caldera formation (Tramparulo et al., 2018), or oblique to strike-slip transfer faults connecting overlapping caldera segments (Natale et al., 2024a), or as observed in analogue model experiments on caldera subsidence (Holohan et al., 2013).

Considering the similarity of directions for the faults formed during the caldera collapse (Vitale et al., 2025) and the faults now bounding the resurgent block, it is reasonable to assume that these structures have been reactivated and inverted during the block resurgence following the MEGT eruption.

5.2. *Dyke structure and dyke-related cataclasis mechanisms*

The analysed dykes exhibit an obsidian core with a perlite structure, surrounded by a cataclastic shell. The perlite structure is defined by an array of glass with varying degrees of hydration (Davis and McPhie, 1996; Cas et al., 2024), which creates spheroids and ellipsoids bounded by concentric fractures. These structures (perlitic cracks) are common in pitchstones and vitrophyres (e.g., Hatch et al., 1983), as well as in pyroclastic deposits (Stewart and McPhie, 2006). When the dyke cools, thermal stresses form concave joints that serve as preferred paths for

fluid migration, allowing water to flow through the glass and trigger the hydration process, thereby forming a perlite structure (von Aulock et al., 2013). The different hydration within the concentric pattern produces distinct stages of perlite crack formation, with some residual non-hydrated obsidian remaining in the core of the kernel. The textural effects of glass hydration depend on both cooling rate and the temperature at which hydration begins (Keller and Pickett, 1954), and the formation of perlite cracks depends on both rapid cooling and hydration (Davis and McPhie, 1996). Rapidly cooled glass subjected to low-temperature hydration undergoes structural rearrangement, leading to contraction and perlitic fracturing. These features are consistent with the formation of glass dykes near the surface, in a host rock that is already lithified and much colder than the intruded magma.

Generally, magmatic dykes are defined by a variety of boundaries, depending on the physical and rheological properties of the magma and host rock (e.g., chemical composition, viscosity, temperature, and stiffness; Geshi et al., 2010; Daniels et al., 2012). Examples of cataclasite associated with dykes intruded in a sedimentary succession, such as a calcareous succession (e.g., Natale et al., 2023). In the case of Ischia Island, the host rock is a tuff characterised by a high porosity (20-49%, Heap et al., 2020), which favours the formation of an irregular boundary between the magma and the tuff. Considering that (i) the magma close to the tuff boundaries undergoes stress shear due to the magma flow and (ii) the shear and tensile strength of tuff are very low (3-4 MPa and 2-4 MPa, respectively; Heap et al., 2021), cataclasis processes can activate along the dyke boundaries. Furthermore, the high thermal gradient between the trachytic magma and the lithified host rock, as previously discussed, and the rapid decrease in magma temperature along the boundaries, favour an increase in viscosity and the development of brittle-ductile deformation mechanisms. As magma begins to solidify and becomes less able to flow, stress builds up until it is released through sudden, brittle failures, such as shear fracturing. The result is a cataclasite in a glassy matrix. In summary, Fig. 11c–g illustrate the conceptual model leading to the formation of a cataclastic zone around the perlitized dyke. First, the magma intrudes within the tuff, characterised by an irregular boundary (Fig. 11c); subsequently, the flowing magma produces drag stress along the boundary, generating a shear zone between tuff and magma, causing cataclasis (Fig. 11d) and comminution (Fig. 11e), and finally solidification (Fig. 11f) and hydration (Fig. 11g) with formation of a perlite structure.

5.3. Petrology

All the analysed dykes exhibit the same mineral assemblage, comparable phenocryst abundance, and equivalent phenocryst, microlite, and groundmass glass compositions. Their major and trace elements whole rock are also similar, indicating that the magma feeding the dykes was chemically homogeneous. The mineralogical assemblage and geochemical characteristics (major and trace elements) closely resemble those of the MEGT (Brown et al., 2008, 2014; D'Antonio et al., 2021) and other Ischia rocks (Melluso et al., 2014; Casalini et al., 2017 and references therein). The dykes described in this study are remarkably similar in textural, mineral assemblage and chemical composition to the samples 0318 (C1 to C7) of Brown et al. (2008, 2014) and D'Antonio et al. (2021), located at Pietra Martone on the west side of Mt. Epomeo (Fig. 12; personal communication Richard Brown; Brown et al., 2008), in a Flow-Unit 2 of the MEGT (the upper intracaldera ignimbrite). This finding is important because it indicates the occurrence of other juvenile obsidian, which we interpreted as dykes, in other locations along the W slope of Mt. Epomeo, and hence supports the interpretation that dykes are not only local magmatic intrusions but are also broadly dispersed along the ring faults bounding the resurgent block. Calcic plagioclase (An_{82-83}), Mg-rich clinopyroxene, and mica phenocrysts identified in the perlitized dyke represent cumulus crystals that were initially separated from the parental mafic melts and subsequently entrained by the ascending trachytic residual magma. These features support an origin of the studied dyke magma through advanced fractional crystallisation of mafic magmas. The absence of olivine in the mineralogical assemblages of the perlitized dykes suggests that the parental mafic melt had relatively evolved. The glass compositions of the studied dykes plot near the trachytic minimum melt (Fig. 10) at a PH_2O of 100 MPa (Hamilton and MacKenzie, 1965). The distribution of Ischia and Campi Flegrei rocks in the Petrogeny Residua system (Fig. 10) indicates independent crystallisation paths of magmas of different compositions.

5.4. Insights into nested caldera structure

According to Vitale et al. (2025), highly deformed ECV deposits at the base of the MEGT, exposed in the study area, indicate deformation associated with caldera collapse. Moreover, the variable thickness of TFS and TME deposits within the caldera (Fig. 1c), with a maximum in the SW sector of the island, suggests that the latter area was likely the depocenter of the nested caldera (Vitale et al., 2025). Furthermore, the Campomanno and Colle Jetto marine sediments, included in the Buceto Syntheme (UCE, Sbrana et al., 2018), and deposited after the MEGT eruption, are confined in the central sector, as reconstructed by Barra et al. (1993), corroborating the occurrence of a nested caldera structure (Fig. 12). Hence, integrating these observations (Vitale et al., 2025) with the novel findings of the present work, we can identify the northern slope of Mt. Epomeo as the location of a ring-fault zone associated with the caldera collapse in the SW sector of the ancient caldera.

Other evidence that strengthens this interpretation is the presence of scoriae and lava lithics within Frassitelli Tuff (ISPRA, 2018) along the northern slope of Mt. Epomeo, and in the Falanga area (Fig. 12). These lithic units belong to the base of the TME, which includes welded scoriae and lithic-rich breccia (Brown et al., 2014; ISPRA, 2018), implying that the area was close to the ignimbrite-erupting vent. Accordingly, our study reported for the first time dykes associated with the nested caldera formation synchronous with the MEGT eruption, such as the petrographic and geochemical analyses illustrated. This indicates that the northern border of the resurgent block was a preferred pathway for upward magma migration at depth, likely along a ring-fault zone. We

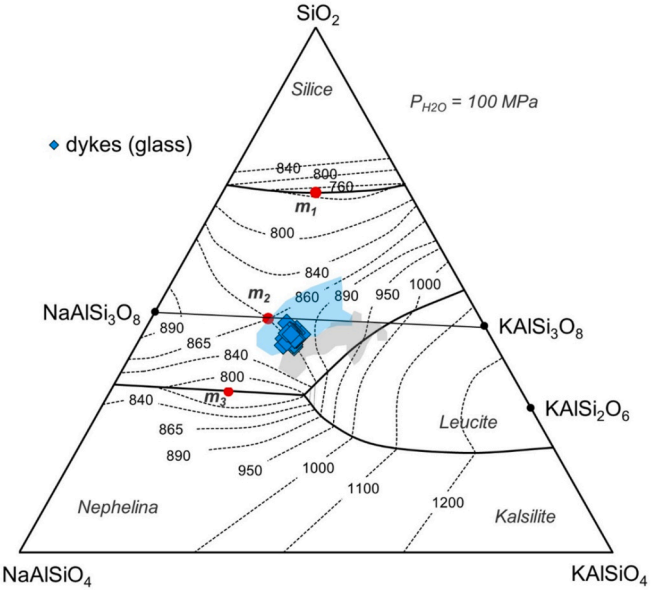

Fig. 10. Petrogeny's Residua System (Hamilton and MacKenzie, 1965) with trachytic glasses of this study. The blue shaded area represents all Ischia evolved rocks (Casalini et al., 2017 and references therein; Melluso et al., 2014; Brown et al., 2008, 2014). The grey shaded area represents the Campi Flegrei evolved rocks (data from Melluso et al., 2012and references therein). (For interpretation of the references to colour in this figure legend, the reader is referred to the Web version of this article.)

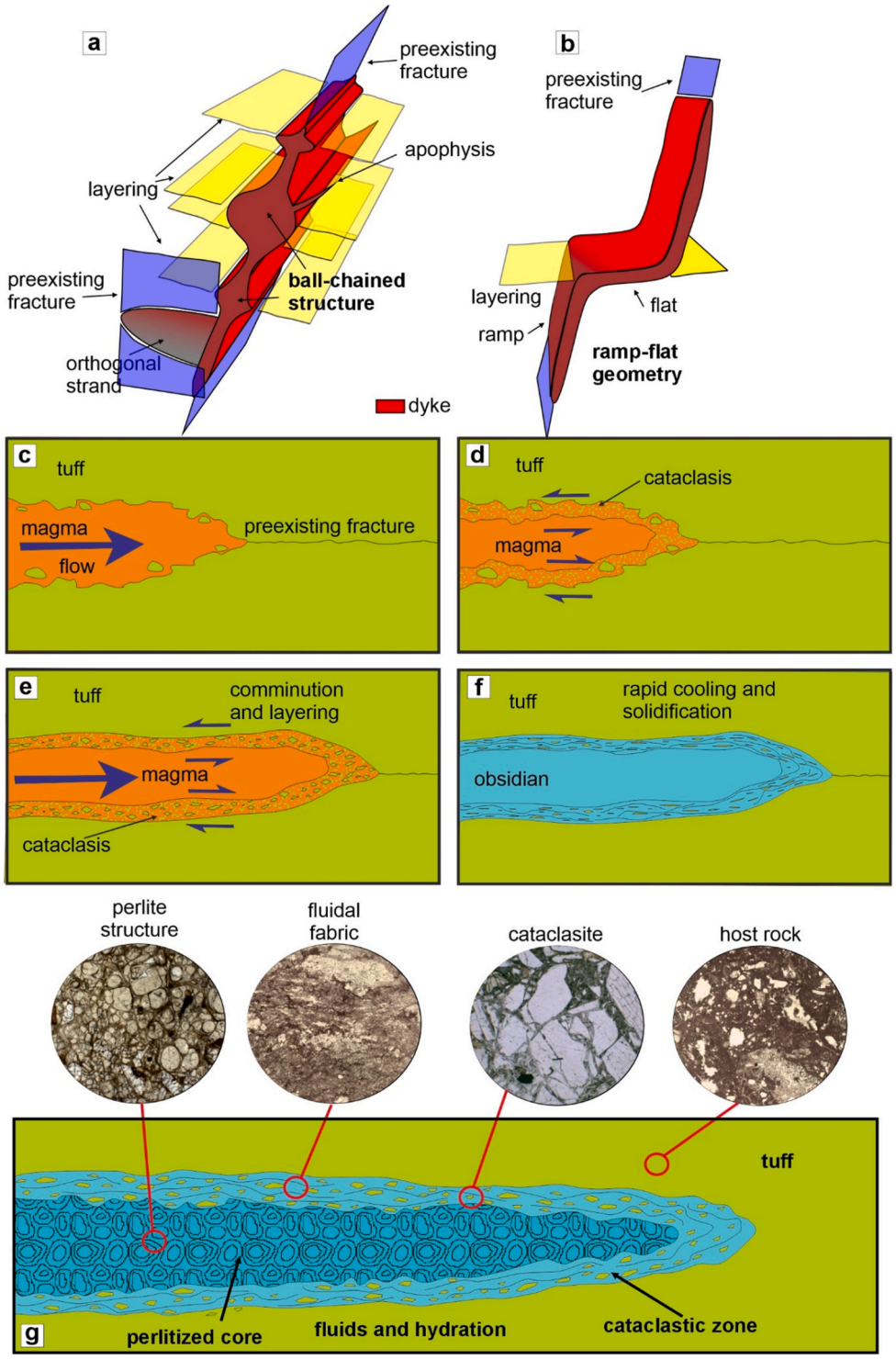

Fig. 11. Models of dyke geometry: (a) ball-chained structure and orthogonal dykes; (b) ramp-flat geometry; (c-f) Cartoons showing the formation of the cataclastic zone around the dyke (the magma flow can be both vertical and horizontal); (g) Sketch of different textures associated with the dyke in the outcropping section.

suggest that near the surface, the ring dykes were injections of magma from a major feeder dyke that fed the MEGT eruption. The intrusion of substantial amounts of magma into circumferential (ring) faults is a common feature in calderas during caldera collapse (e.g., Saunders, 2005 and references therein).

Indeed, inclined sheets, departing from a deep reservoir, can encounter the ring fault and be deflected into it (Browning and Gudmundsson, 2015; Natale et al., 2026a,b).

As described earlier, the fault displacements in the ring zone can reach tens of meters; in contrast, the dyke thicknesses are very small, up to a few tens of centimetres in the ball-chained structures.

Thus, these dyke fingers record the intrusion of volatile-poor magma into pre-existing structural fabric, including fractures and layering (Pollard et al., 1975). These intrusions likely remained blind and did not erupt, whereas larger and more laterally extensive dykes elsewhere along the ring fault zone acted as feeders for the TME ignimbrite eruption. It is important to emphasise that the studied area is a small portion of the caldera; however, as described previously, similar structures have

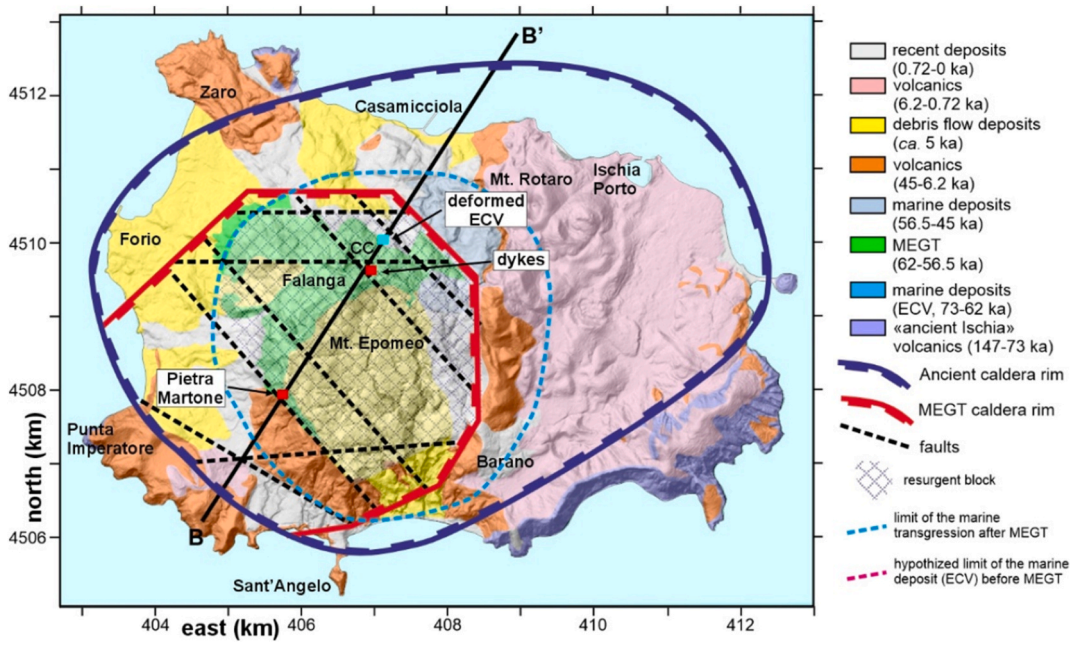

Fig. 12. Schematic geological map showing the limits of the resurgent block, marine ingression post-MEGT, ECV deposits, and the outer rim of the ancient caldera (modified after Vitale et al., 2025). CC: Cava Celario.

been observed at the Pietra Martone locality (Fig. 12). Unfortunately, there are no other outcrops because the entire northern slope of Mt. Epomeo is covered by deposits from ancient and more recent landslides, dense vegetation, and urbanization, which prevent the bedrock tuffs from being exposed. The 2022 landslide allowed us to properly observe these magmatic dykes and their geometries for the first time. Therefore, in the following proposed model, we will draw inferences from observations on the northern and western slopes of Mt. Epomeo (including the study area and the Pietra Martone locality), recognising that this may not be representative of the entire caldera. Still, these are the only data available in the literature to depictinsights into the caldera's structure. Hence, to illustrate the previously discussed volcano-tectonic features, we sketched (i) the rim of the ancient caldera in Fig. 12, based on the outcrop limits of the marine/lacustrine deposits of ECV before the MEGT eruption, (ii) the marine ingression following the MEGT eruption, and (iii) the resurgent block. The figure also shows the post-MEGT volcanic deposits and the major faults within the nested structure (Vitale et al., 2025). All these features, joined with (i) the occurrence along the northern slope of the Mt. Epomeo of deformation consistent with a caldera collapse (Vitale et al., 2025), (ii) obsidian dykes associated with MEGT eruption, and (iii) evidence of vent-near products at the Falanga area (ISPRA, 2018), suggest that the SW area of the ancient caldera hosted a nested subcircular caldera structure, formed with the MEGT event, which, therefore, have produced a caldera significantly smaller than the "ancient" one (Fig. 12).

5.5. Block resurgence mechanism

Different models have been proposed to the resurgence of Mt. Epomeo. All converge towards the intrusion of a magma body in shallow crustal levels, triggering uplift (Fusi et al., 1990; Orsi et al., 1991; Cubellis and Luongo, 1998; Acocella et al., 1997; Acocella and Funiciello, 1999; Molin et al., 2003; Sbrana et al., 2009; Carlino, 2012). Orsi et al. (1991) presented a "simple shear model" characterised by a vertical extrusion confined by reverse faults in the NW edge of the resurgent block and normal faults at the SE part. The authors suggest that the faults are likely the result of the reactivation of pre-existing caldera fractures. Acocella and Funiciello (1999) proposed a slightly different model, defined by the tilting of the Mt. Epomeo block, with the hinge localised in the SE sector and reverse faults in the NW part ("trap-door model"). In both models, the block is bounded by inward faults. Molin et al. (2003) refined the previous model through analogical modelling, indicating the role of outward-normal faults along the NW slope in gravitational collapse. In contrast, Carlino (2012) proposed that a block resurgence driven by the intrusion of a laccolite was allowed by the only activity of outward normal faults along the northern and southern sectors. However, this latter model works only if an extensional stress field with σ3-oriented NW-SE is considered. In all models, the NW-SE boundary faults of the resurgent block behave as transfer structures.

The structural survey conducted in this study reveals the presence of high-angle inward- and outward-normal faults along the NW slope of Mt. Epomeo, with displacements of a few meters. However, the major fault structures in this sector are buried beneath older and recent debris flows, landslides, and colluvial and alluvial deposits (ISPRA, 2018). These hidden faults exhibit displacements of several hundred meters, as illustrated in the map and cross-section (Fig. 1a and b) and documented in official geological cartography (ISPRA, 2018). These structures include the E-W fault zone bounding the northern side of Mt. Epomeo and the two major NW-SE-directed faults bounding the NE sector of Mt. Epomeo. The results of our study suggest that most of the displacement was recorded by a few structures synchronously with diffuse faulting, including almost vertical, outward and inward faults. In this scenario, the observed transtensive and strike-slip faults acted as transfer shear planes between different segments of dip-slip faults. Due to the close relationships between the observed faults and the ring fault zone reconstructed in this work and in Vitale et al. (2025), we suggest that the resurgent block reactivated the ring faults of the innermost caldera, locally inverting them, at least in the northern sector; in particular, the structures located on the northern side were reactivated both with normal and reverse kinematics. Finally, integrating these findings, we propose a volcano-tectonic evolution model of Ischia Island (Fig. 13) along a cross-section B-B' (Fig. 12).

The formation of the ancient caldera likely occurred between 90 and 110 ka, based on the age of the oldest rocks, and is tentatively correlated to widely dispersed tephra markers of Ischia-like compositions identified across the Mediterranean, with modelled ages of ~96 and 104 ka (Fernandez et al., 2024, and references therein) and associated with large explosive eruptions. After (Fig. 13a), the marine sediments of ECV

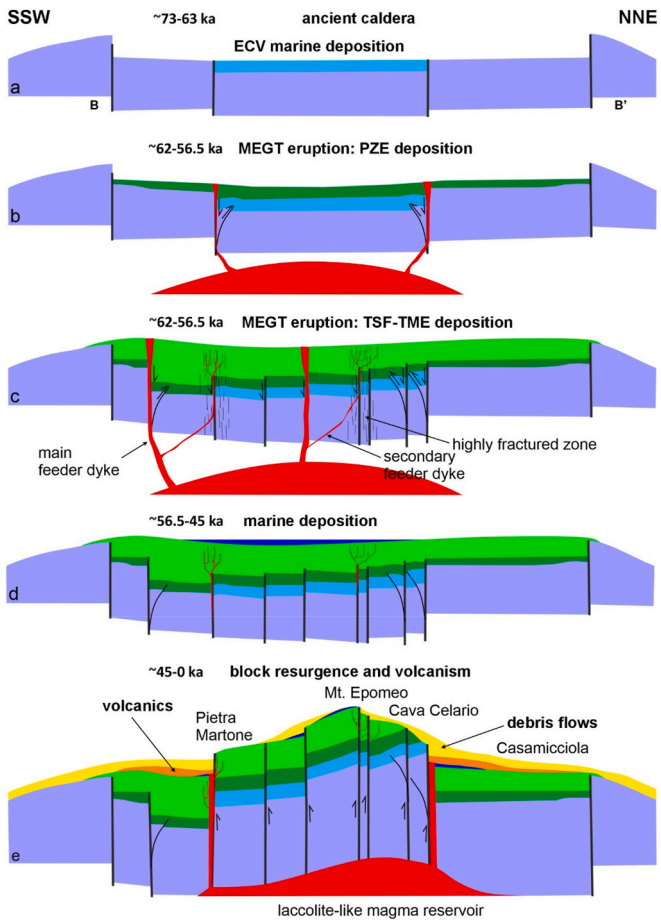

Fig. 13. Cartoon showing the volcano-tectonic evolution of Ischia Island. (a) ECV marine deposition in the ancient caldera (~73-63 ka); (b) reactivation of the caldera with the PZE eruption filling the ancient caldera floor (~62-56.5 ka); (c) TFS and TME eruption and formation of a nested caldera in the SW sector of the island (~62-56.5 ka); (d) deposition of marine to continental deposits in the caldera centre (~56.5-45 ka); (d) block resurgence, volcanism and debris flow formation 45 ka-today). Not to scale. The thicknesses of dykes have been exaggerated.

were deposited in the central sector. However, we can only hypothesise a nested caldera structure that formed a central depression, filled with reworked volcanic deposits. In the interval ~62-56.5 ka, the first MEGT eruption stage was characterised by the deposition of the PZE within the ancient caldera (Fig. 13b). Subsequently, the second stage of the MEGT eruption was defined by the collapse of the SW sector, marked by a strong deformation of ECV deposits, and the occurrence of obsidian dykes and vent proximal deposits. TFS and TME were deposited in this stage, filling the depocenter and the remnant of the ancient caldera depression. After the MEGT eruption and formation of a nested structure (Fig. 13c), the caldera centre became the site of marine ingression and deposition of reworked volcanic sediments (Fig. 13d). Meanwhile, the central sector was affected by a dome-like uplift, and from 45 ka, by a resurgent block uplift (Fig. 13e), reactivating the pre-existing ring faults. The resurgence was punctuated by subsidence periods characterised by volcanic activity and slope instability, triggering large debris flows. The doming and block resurgent were likely driven by the emplacement of a laccolith-like magma body (Carlino, 2012; Vitale et al., 2025).

6. Conclusions

The new exposures of the deepest caldera-fill rocks on Ischia Island, revealed by the 2022 Casamicciola landslide, have allowed direct investigation of caldera-related structures, such as ring-faults and magmatic dykes. The resurgence of Mt. Epomeo provided a unique opportunity to examine deformation features that were previously buried beneath the caldera infill, including the Mt. Epomeo Green Tuff (MEGT) sequence.

Structural survey conducted in the Cava Celario outcrop revealed the existence of magmatic dykes within the medial part (Frassitelli Tuff) of the MEGT deposits (62 and 56.5 ka). The dykes occur along the northern slope of the resurgent block of Mt. Epomeo, in the central part of the Island. Dykes are typically thin (generally <20 cm), lens-shaped bodies with a ball-chained geometry. Dykes consist of an obsidian core with a perlitic texture, containing phenocrysts of sanidine, plagioclase, clinopyroxene, mica, and opaque oxides. The core is enclosed in a cataclasite with a glassy matrix.

Petrological analysis indicates that dykes have trachytic composition identical in major and trace elements to the MEGT rocks, confirming a genetic link to the final phase of the MEGT eruption. Textural and compositional features suggest that crystallisation began at shallow depth and continued during magma ascent. Our results indicate that the trachytic magma formed at temperatures of approximately 850-950 °C and with relatively high water content (approximately 5 wt% H_2O).

The occurrence of cataclasites embedding the obsidian core indicates that the magmatic intrusion was accompanied by brittle deformation of the tuff host rock, a relatively uncommon feature of magmatic intrusions. Based on dyke geometries, we infer that emplacement occurred along pre-existing structures associated with the caldera collapse in the southwestern sector of Ischia. The studied dykes therefore represent shallow magma injection along a ring fault zone, with magma rapidly cooling as it approached the surface, forming obsidian. Finally, the structural survey of faults bounding the northern slope of Mt. Epomeo indicates a similar pattern of structures, suggesting that the resurgent block reactivated and inverted pre-existing ring-faults in this sector of the caldera. This work, in combination with the existing literature, helps redefine the intricate volcano-tectonic structure of Ischia Island, disentangling its complex evolution which profoundly affects dynamic behaviour and seismicity.

CRediT authorship contribution statement

Stefano Vitale: Writing – review & editing, Writing – original draft, Visualization, Investigation, Formal analysis, Data curation, Conceptualization. **Daniele Morgavi:** Writing – review & editing, Writing – original draft, Validation, Methodology, Investigation, Formal analysis. **Ciro Cucciniello:** Writing – review & editing, Writing – original draft, Visualization, Validation, Methodology, Investigation, Formal analysis, Data curation, Conceptualization. **Jacopo Natale:** Writing – review & editing, Visualization, Validation, Methodology, Conceptualization. **Thomas Lemaire:** Formal analysis. **Mubashir Mehmood:** Writing – review & editing, Validation, Methodology, Formal analysis. **Fabrizio Di Fiore:** Writing – review & editing, Validation, Methodology, Formal analysis. **Lorenzo Benedetto:** Investigation. **Sabatino Ciarcia:** Writing – review & editing, Supervision, Investigation, Formal analysis.

Declaration of competing interest

The authors declare that they have no known competing financial interests or personal relationships that could have appeared to influence the work reported in this paper.

Acknowledgements

We thank the Editor Irene Raposo for the careful handling of the submission, the reviewer Gudmundsson and the anonymous reviewer for their constructive suggestions and criticism, which have greatly strengthened the manuscript. The authors thank Sergio Bravi for preparing the thin sections and Roberto de' Gennaro for assistance in the

SEM-EDS laboratory. The Authors are very grateful to Richard Brown, Ilenia Arienzo, and Massimo D'Antonio for providing valuable information on the outcrop and sample locations of their works.

This work was supported by "Convenzioni tra il Commissario Straordinario per la ricostruzione nei territori dell'Isola d'Ischia interessati dal sisma del 21 agosto 2017 e DiSTAR – UNINA (responsabile Prof. Domenico Calcaterra) e DST-UNISANNIO (responsabile Prof.ssa Paola Revellino)". Grant number [CUP E63C23001090001] and by the Istituto Nazionale di Geofisica e Vulcanologia, Italy, grant microanalysis, Experimental pEtrology and numerical modellinG to unravel the precursor phenomena Of voLcanic eruptions: the case of the Neapolitan volcanoes - SMEEGOL" (Resp. Dott. I. Arienzo) - code CUP D53J19000170001, funded by Italian Ministry MIUR ("Fondo Finalizzato al rilancio degli investimenti delle amministrazioni centrali dello Stato e allo sviluppo del Paese". The University of Bari "Aldo Moro" is acknowledged for granting the Open Access in the framework of CARE-CRUI agreement with Elsevier.

Appendix A. Supplementary data

Supplementary data to this article can be found online at https://doi.org/10.1016/j.jsg.2026.105655.

Data availability

Data will be made available on request.

References

Acocella, V., Funiciello, R., Lombardi, S., 1997. Active tectonics and resurgence at Ischia Island (southern Italy). Alpine and Mediterranean Quaternary 10 (2), 427–432.

Acocella, V., Funiciello, R., 1999. The interaction between regional and local tectonics during resurgent doming: the case of island of Ischia, Italy. J. Volcanol. Geoth. Res. 88, 109–123.

Allgood, C., Llewellin, E.W., Brown, R.J., Loisel, A., 2025. Magma flow localisation during dyke propagation produces complex magma transport pathways. Nat. Commun. 16, 6358. https://doi.org/10.1038/s41467-025-61620-5.

Brown, R.J., Orsi, G., de Vita, S., 2008. New insights into late Pleistocene explosive volcanic activity and caldera formation on ischia (Southern Italy). Bull. Volcanol. 70 (5), 583–603. https://doi.org/10.1007/s00445-007-0155-0.

Brown, R., Civetta, L., Arienzo, I., D'Antonio, M., Moretti, R., Orsi, G., Tomlinson, E.L., Albert, P.G., Menzies, M., 2014. Assembly, evolution and disruption of a magmatic plumbing system before and after a cataclysmic caldera-collapse eruption at Ischia volcano (Italy). Contrib. Mineral. Petrol. 168, 1035.

Browning, J., Gudmundsson, A., 2015. Caldera faults capture and deflect inclined sheets: an alternative mechanism of ring dike formation. Bull. Volcanol. 77 (1), 4.

Caputo, R., 1995. Evolution of orthogonal sets of coeval extension joints. Terra Nova 7 (5), 479–490.

Carlino, S., 2012. The process of resurgence for Ischia Island (Southern Italy) since 55 Ka: the Laccolith model and implications for eruption forecasting. Bull. Volcanol. 74 (5), 947–961. https://doi.org/10.1007/s00445-012-0578-0.

Carlino, S., Sbrana, A., Pino, N.A., Marianelli, P., Pasquini, G., De Martino, P., De Novellis, V., 2022. The volcano-tectonics of the Northern sector of Ischia Island caldera (Southern Italy): resurgence, subsidence and earthquakes. Front. Earth Sci. 10, 730023.

Cas, R., Giordano, G., Wright, J.V., 2024. Volcanology: Processes, Deposits, Geology and Resources. Springer International Publishing, Cham, Switzerland.

Casalini, M., Avanzinelli, R., Heumann, A., de Vita, S., Sansivero, F., Conticelli, S., Tommasini, S., 2017. Geochemical and radiogenic isotope probes of Ischia volcano, Southern Italy: constraints on magma chamber dynamics and residence time. Am. Mineral. 102 (2), 262–274. https://doi.org/10.2138/am-2017-5724.

Ciarcia, S., Vitale, S., 2025. Orogenic evolution of the northern Calabria-southern Apennines system in the framework of the Alpine chains in the central-western Mediterranean area. GSA Bull. 137 (3-4), 1143–1176. https://doi.org/10.1130/B37474.1.

Cole, J.W., Nilner, D.M., Spudis, K.D., 2005. Calderas and caldera structures: a review. Earth Sci. Rev. 69, 1–26.

Cubellis, E., Luongo, G., 1998. Il contesto fisico. In: Il Terremoto Del 28 Luglio 1883 a Casamicciola Nell'Isola D'Ischia. Istituto Poligrafico e Zecca Dello Stato, Rome, Italy, pp. 49–123.

Cucciniello, C., Grifa, C., le Roex, A.P., de Gennaro, R., Morra, V., Melluso, L., 2023. Feeding system and mantle sources of the southern and western sector of the Madagascar flood basalt province, and comparisons with Southwest Indian Ridge "anomalous" basalts. Lithos 458–459, 107361.

Daniels, K.A., Kavanagh, J.L., Menand, T., Stephen, J.S.R., 2012. The shapes of dikes: evidence for the influence of cooling and inelastic deformation. GSA Bull. 124 (7–8), 1102–1112.

D'Antonio, M., Arienzo, I., Brown, R.J., Petrosino, P., Pelullo, C., Giaccio, B., 2021. Petrography and mineral chemistry of Monte Epomeo Green Tuff, Ischia Island, South Italy: constraints for identification of the Y-7 tephrostratigraphic marker in distal sequences of the central Mediterranean. Minerals 11, 955. https://doi.org/10.3390/min11090955.

Davis, B., McPhie, J., 1996. Spherulites, quench fractures and relict perlite in a late Devonian rhyolite dyke, Queensland, Australia. J. Volcanol. Geoth. Res. 71, 1–11.

Della Seta, M., Marotta, E., Orsi, G., de Vita, S., Sansivero, F., Fredi, P., 2012. Slope instability induced by volcano-tectonics as an additional source of hazard in active volcanic areas: the case of Ischia island (Italy). Bull. Volcanol. 74, 79–106.

De Novellis, V., Carlino, S., Castaldo, R., Tramelli, A., De Luca, C., Pino, N.A., Pepe, S., Convertito, V., Zinno, I., De Martino, P., Bonano, M., Giudicepietro, F., Casu, F., Macedonio, G., Manunta, M., Cardaci, C., Manzo, M., Di Bucci, D., Solaro, G., Zeni, G., Lanari, R., Bianco, F., Tizzani, P., 2018. The 21 August 2017 ischia (Italy) earthquake source model inferred from seismological, GPS, and DInSAR measurements. Geophys. Res. Lett. 45, 2193–2202.

de Vita, S., Sansivero, F., Orsi, G., Marotta, E., Piochi, M., 2010. Volcanological and structural evolution of the ischia resurgent caldera (Italy) over the past 10 Ka. GSA Special Papers 464, 193–239.

Di Fiore, F., Mollo, S., Vona, A., MacDonald, A., Ubide, T., Nazzari, M., Romano, C., Scarlato, P., 2021. Kinetic partitioning of major and trace cations between clinopyroxene and phonotephritic melt under convective stirring conditions: new insights into clinopyroxene sector zoning and concentric zoning. Chem. Geol. 584, 120531. https://doi.org/10.1016/j.chemgeo.2021.120531.

Diamanti, R., Camanni, C., Natale, J., Vitale, S., 2022. A gravitational origin for volcano-tectonic faults in the Campi Flegrei caldera (southern Italy) inferred from detailed field observations. J. Struct. Geol., 104671 https://doi.org/10.1016/j.jsg.2022.104671.

Fernandez, G., Giaccio, B., Costa, A., Monaco, L., Nomade, S., Albert, P., Pereira, A., Flynn, M., Leicher, N., Lucchi, F., Petrosino, P., Palladino, D.M., Milia, A., Insinga, D. D., Wulf, S., Kearney, R., Veres, D., Jordanova, D., Putignano, M.L., et al., 2024. New constraints on the middle-late Pleistocene Campi Flegrei explosive activity and Mediterranean tephrostratigraphy (~160 ka and 110-90 ka). Quat. Sci. Rev. 331, 108623.

Fusi, N., Tibaldi, A., Vezzoli, L., 1990. Vulcanismo, risorgenza calderica e relazioni con la tettonica regionale nell'isola d'Ischia. Memorie Società Geologica Italiana 45, 971–980.

Galindo, I., Gudmundsson, A., 2012. Basaltic feeder dykes in rift zones: geometry, emplacement, and effusion rates. Nat. Hazards Earth Syst. Sci. 12, 3683–3700. https://doi.org/10.5194/nhess-12-3683-2012.

Galvani, A., Pezzo, G., Sepe, V., Ventura, G., 2021. Shrinking of Ischia Island (Italy) from long-term geodetic data: implications for the deflation mechanisms of resurgent calderas and their relationships with seismicity. Remote Sens. 13 (22), 4648.

Geshi, N., Kusumoto, S., Gudmundsson, A., 2010. Geometric difference between non-feeder and feeder dikes. Geology 38 (3), 195–198.

Geyer, A., Martí, J., 2009. Stress fields controlling the formation of nested and overlapping calderas: implications for the understanding of caldera unrest. J. Volcanol. Geothermal Res. 181 (3–4), 185–195.

Guarino, V., Solone, R., Casalini, M., Franciosi, L., Dallai, L., Morra, V., Conticelli, S., Melluso, L., 2024. The geochemistry of leucite-bearing lavas from early stages of the Somma-Vesuvius volcanic complex: feeder systems and mantle enrichment processes in the Neapolitan district of the Roman Magmatic Province. Geochemistry 84 (1), 126076. https://doi.org/10.1016/j.chemer.2023.126076.

Gudmundsson, A., 1984. Formation of dykes, feeder-dykes, and the intrusion of dykes from magma chambers. Bull. Volcanol. 47, 537–550.

Gudmundsson, A., 1988. Formation of collapse calderas. Geology 16 (9), 808–810.

Gudmundsson, A., 2007. Conceptual and numerical models of ring-fault formation. J. Volcanol. Geoth. Res. 164, 142–160.

Gudmundsson, A., 2016. The mechanics of large volcanic eruptions. Earth Sci. Rev. 163, 72–93.

Gudmundsson, A., 2020. Volcanotectonics: Understanding the Structure, Deformation and Dynamics of Volcanoes. Cambridge University Press.

Gudmundsson, A., 2022. The propagation paths of fluid-driven fractures in layered and faulted rocks. Geol. Mag. 1–24.

Hamilton, D.L., MacKenzie, W.S., 1965. Phase equilibrium studies in the system NaAlSiO4 (nepheline) – KalSiO4 (kalsilite)– SiO2 –H2O. Mineral. Mag. 34, 214–231.

Hatch, F.H., Wells, A.K., Wells, M.K., 1983. Petrology of the Igneous Rocks, thirteenth ed. Thomas Murby, London.

Heap, M.J., Wadsworth, F.B., Heng, Z., Xu, T., Griffiths, L., Velasco, A.A., Vairé, E., Vistour, M., Reuschlé, T., Troll, V.R., Deegan, F.M., Tang, C.A., 2021. The tensile strength of volcanic rocks: experiments and models. J. Volcanol. Geoth. Res. 418, 107348.

Heap, M.J., Villeneuve, M., Albino, F., Farquharson, J.I., Brothelande, E., Amelung, F., et al., 2020. Towards more realistic values of elastic moduli for volcano modelling. J. Volcanol. Geoth. Res. 390, 106684.

Hobé, A., Bazargan, M., Selek, B., Tryggvason, A., Alofe, E., Gudmundsson, A., 2025. Tomographic and volcanotectonic controls on the 2021–2023 Fagradalsfjall eruptions, Iceland. Sci. Rep. 15, 16455.

ISPRA (Istituto superiore per la protezione e la ricerca ambientale), 2018. Geological Maps of Italy, Sheet 464 Isola D'Ischia Scale 1:50.000. ISPRA, Rome, Italy. https://www.isprambiente.gov.it/Media/carg/464_ISOLA_DISCHIA/Foglio.html. (Accessed 31 May 2025).

Iovine, R.S., Mazzeo, F.C., Arienzo, I., D'Antonio, M., Wörner, G., Civetta, L., et al., 2017. Source and magmatic evolution inferred from geochemical and Sr-O-isotope data on hybrid lavas of Arso, the last eruption at Ischia island (Italy; 1302 AD). J. Volcanol. Geoth. Res. 331, 1–15.

Keller, W.D., Pickett, E.E., 1954. Hydroxyl and water in perlite from Superior, Arizona. Am. J. Sci. 252, 87–98.
Kennedy, B.M., Holohan, E.P., Stix, J., Gravley, D.M., Davidson, J.R., Cole, J.W., Burchardt, S., 2018. Volcanic and igneous plumbing systems of caldera volcanoes. In: Burchardt, S. (Ed.), Volcanic and Igneous Plumbing Systems. Elsevier, pp. 259–284.
Le Maitre, R.W., 2002. Igneous rocks: a classification and glossary of terms. Recommendations of the International Union of Geological Sciences Subcommission on the Systematics of Igneous Rocks. Cambridge University Press, Cambridge.
Manzo, M., Ricciardi, G.P., Casu, F., Ventura, G., Zeni, G., Borgström, S., et al., 2006. Surface deformation analysis in the Ischia Island (Italy) based on spaceborne radar interferometry. J. Volcanol. Geoth. Res. 151 (4), 399–416.
Martí, J., Gudmundsson, A., 2000. The Las Cañadas caldera (Tenerife, Canary Islands): an overlapping collapse caldera generated by magma-chamber migration. J. Volcanol. Geoth. Res. 103 (1-4), 161–173.
Martí, J., Geyer, A., Folch, A., Gottsmann, J., 2008. A review on collapse caldera modelling. In: Marti, J., Gottsmann, J. (Eds.), Caldera Volcanism: Analysis, Modelling and Response. Developments in Volcanology 10. Elsevier, pp. 233–283.
Masotta, M., Mollo, S., 2019. A new plagioclase-liquid hygrometer specific to trachytic systems. Minerals 9, 375. https://doi.org/10.3390/min9060375.
McKee, C.O., Duncan, R.A., 2016. Early volcanic history of the Rabaul area. Bull. Volcanol. 78, 1–28.
Melluso, L., De'Gennaro, R., Fedele, L., Franciosi, L., Morra, V., 2012. Evidence of crystallization in residual, Cl–F-rich, agpaitic, trachyphonolitic magmas and primitive Mg-rich basalt–trachyphonolite interaction in the lava domes of the Phlegrean Fields (Italy). Geol. Magaz. 149 (3), 532–550.
Melluso, L., Morra, V., Guarino, R., de' Gennaro, R., Franciosi, L., Grifa, C., 2014. The crystallization of shoshonitic to pralkaline trachyphonolitic magmas in a H2O-Cl-F-rich environment at Ischia (Italy), with implications for the feeder system of the Campania Plain volcanoes. Lithos 210, 242–259.
Mollo, S., Di Fiore, F., MacDonald, A., Ubide, T., Pontesilli, A., Giuliani, G., Vona, A., Romano, C., Scarlato, P., 2024. Thermodynamics and kinetics of cation partitioning between plagioclase and trachybasaltic melt in static and dynamic systems: a reassessment of the lattice strain and electrostatic energies of substitution. Geochem. Cosmochim. Acta 384, 27–43. https://doi.org/10.1016/j.gca.2024.09.006.
Mollo, S., Masotta, M., Forni, F., Bachmann, O., De Astis, G., Moore, G., Scarlato, P., 2015. A K-feldspar–liquid hygrometer specific to alkaline differentiated magmas. Chem. Geol. 392, 1–8.
Molin, P., Acocella, V., Funiciello, R., 2003. Structural, seismic and hydrothermal features at the border of an active intermittent resurgent block: ischia Island (Italy). J. Volcanol. Geoth. Res. 121 (1-2), 65–81.
Natale, J., Camanni, G., Ferranti, L., Isaia, R., Sacchi, M., Spiess, V., Steinmann, L., Vitale, S., 2022. Fault systems in the offshore sector of the Campi Flegrei caldera (southern Italy): implications for nested caldera structure, resurgent dome, and volcano-tectonic evolution. J. Struct. Geol. 163, 104723.
Natale, J., Vitale, S., Giordano, G., Fedele, L., Lucci, F., Vona, A., Prinzi, E.P., Tramparulo, F.d.A., Isaia, R., Ciarcia, S., 2023. The taverna San felice dike (NE of Roccamonfina Volcano): unraveling magmatic intrusion processes and volcano-tectonics in the tyrrhenian Margin of the Southern apennines. G-cubed 24 (8). https://doi.org/10.1029/2023GC010994 e2023GC010994.
Natale, J., Vitale, S., Giordano, G., Jicha, B., Morra, V., 2026a. Uncovering the Middle–Late Pleistocene slip history of Garigliano Graben faults and its impact on the construction and collapse of the Roccamonfina volcano, Italy. Geol. Soc. London, Special Publicat. 560 (1) gslspecpub2024-g2054.
Natale, J., Vitale, S., Isaia, R., 2024a. Simultaneous normal and reverse faulting in reactivating caldera faults: a detailed field structural analysis from Campi Flegrei (southern Italy). J. Struct. Geol. 181, 105109.
Natale, J., Vitale, S., Repola, L., Monti, L., Isaia, R., 2024b. Geomorphic analysis of digital elevation model generated from vintage aerial photographs: a glance at the pre-urbanization morphology of the active Campi Flegrei caldera. Geomorphology 460, 109267.
Natale, J., Cascella, E., Vitale, S., 2026b. Tracking the growth and deformation of fissure phreatomagmatic eruptions: insights from the ca. 3.9 ka Nisida eruption at Campi Flegrei caldera, southern Italy. Geol. Soc. Am. Bull. 138 (1-2), 445–468. https://doi.org/10.1130/B38367.1, 2026.
Nimis, P., 1999. Clinopyroxene geobarometry of magmatic rocks. Part 2. Structural geobarometers for basic to acid, tholeiitic and mildly alkaline magmatic systems. Contrib. Mineral. Petrol. 135, 62–74.
Orsi, G., Gallo, G., Zanchi, A., 1991. Simple-shearing block resurgence in caldera depressions. A model from Pantelleria and Ischia. J. Volcanol. Geoth. Res. 47 (1-2), 1–11.
Orsi, G., 2022. Volcanic and deformation history of the Campi Flegrei volcanic field, Italy. In: Orsi, G., D'Antonio, M., Civetta, L. (Eds.), Campi Flegrei: a Restless Caldera in a Densely Populated Area. Springer, Berlin, Heidelberg, pp. 1–53.
Peccerillo, A., Taylor, S.R., 1976. Geochemistry of Eocene calc-alkaline volcanic rocks of the Kastamonu area, northern Turkey. Contrib. Mineral. Petrol. 58, 63–81.
Pollard, D.D., Muller, O.H., Dockstader, D.R., 1975. The form and growth of fingered sheet intrusions. Geol. Soc. Am. Bull. 86, 351–363.
Putirka, K.D., 2008. Thermometers and barometers for volcanic systems. Rev. Mineral. Geochem. 69, 61–120.
Romeo, S., D'Angiò, D., Fraccica, A., Licata, V., Vitale, V., Chiessi, V., Amanti, M., Bonasera, M., 2023. Investigation and preliminary assessment of the Casamicciola landslide in the island of Ischia (Italy) on November 26, 2022. Landslides 20, 1265–1276.
Sbrana, A., Fulignati, P., Marianelli, P., Boyce, A.J., Cecchetti, A., 2009. Exhumation of an active magmatic-hydrothermal System in a resurgent caldera environment: the example of ischia (Italy). J. Geol. Soc. 166, 1061–1073.
Sbrana, A., Marianelli, P., Pasquini, G., 2018. Volcanology of ischia (Italy). J. Maps 14 (2), 494–503.
Silva-Fragoso, A., Norini, G., Nappi, R., Groppelli, G., Michetti, A.M., 2024. Improving the accuracy of digital terrain models using drone-based LiDAR for the morpho-structural analysis of active calderas: the case of Ischia Island, Italy. Remote Sens. 16 (11), 1899.
Stewart, A.L., McPhie, J., 2006. Facies architecture and Late Pliocene–Pleistocene evolution of a felsic volcanic island, Milos, Greece. Bull. Volcanol. 68 (7), 703–726.
Tramparulo, F.D.A., Vitale, S., Isaia, R., Tadini, A., Bisson, M., Prinzi, E.P., 2018. Relation between alternating open/closed-conduit conditions and deformation patterns: an example from the Somma-Vesuvius volcano (southern Italy). J. Struct. Geol. 112, 138–153. https://doi.org/10.1016/j.jsg.2018.05.008. ISSN: 0191-8141.
Vezzoli, L., Principe, C., Malfatti, J., Arrighi, S., Tanguy, J.C., Le Goff, M., 2009. Modes and times of caldera resurgence: the< 10 ka evolution of Ischia Caldera, Italy, from high-precision archaeomagnetic dating. J. Volcanol. Geoth. Res. 186 (3-4), 305–319.
Vitale, S., Aiello, G., Barano, U., Barra, B., Morgavi, M., Natale, J., Parisi, R., Ciarcia, S., 2025. Ring fault-related deformation mechanisms in active calderas: new insights from a deep section of the Mt. Epomeo Green Tuff resurgent block (Ischia Island). Bull. Volcanol. 87, 45. https://doi.org/10.1007/s00445-025-01828-x.
Von Aulock, F.W., Nichols, A.R.L., Kennedy, B.M., Oze, C., 2013. Timescales of texture development in a cooling lava dome. Geochem. Cosmochim. Acta 114, 72–80.
Walker, G.P., 1984. Downsag calderas, ring faults, caldera sizes, and incremental caldera growth. J. Geophys. Res. Solid Earth 89 (B10), 8407–8416.